Quantifying Astronaut Tasks: Robotic Technology and Future Space Suit Design

PI: Professor Dava Newman
Final Report, NASA, NAG9-1089
May 30, 2003

Table of Contents

1.0 Introduction

Since the first extravehicular activities (EVAs) were performed by Alexei Leonov and Ed White in 1965, the capabilities of astronauts to do useful work outside of their spacecraft have steadily increased. Likewise, our understanding of EVA astronauts' capabilities and limitations have also progressed through inflight experience, experimentation in neutral buoyancy facilities and parabolic flight, and engineering tests of space suits and EVA tools. The purpose of this research effort is to further advance the current understanding of astronauts' capabilities and limitations in space-suited EVA.

The most important aspect of an EVA astronaut's capabilities is the ability to move his or her body while wearing the space suit. In every EVA scenario, astronauts physically manipulate objects to accomplish tasks. Two factors make these physical interactions strikingly different from those performed on the ground. First, the microgravity environment requires an astronaut to restrain his or her body in order to exert forces and moments on another object, and second, space suits constrain astronauts' body motions in significant and complicated ways.

Historically, feasible limits on planned EVA activities have been determined based on ground experimentation and in-flight experience. Data have been obtained experimentally on operational performance metrics such as joint ranges of motion, the volume in space that a space-suited astronaut can reach, known as the reach envelope, the subset of the reach envelope in which a space-suited astronaut can comfortably work, known as the work envelope, and the strength of a suited astronaut. These performance measures are related to each other through the constitutive and compatibility relations that govern the space suit's behavior, but isolated experimental data does not allow one performance measure to be predicted from another or the same performance measure to be generalized to a different person or situation.

The primary aim of this research effort was to advance the current understanding of astronauts' capabilities and limitations in space-suited EVA by developing models of the constitutive and compatibility relations of a space suit, based on experimental data gained from human test subjects as well as a 12 degree-of-freedom human-sized robot, and utilizing these fundamental relations to estimate a human factors performance metric for space suited EVA work. The three specific objectives are to:

1. Compile a detailed database of torques required to bend the joints of a space suit, using realistic, multi-joint human motions.
2. Develop a mathematical model of the constitutive relations between space suit joint torques and joint angular positions, based on experimental data and compare other investigators' physics-based models to experimental data.
3. Estimate the work envelope of a space suited astronaut, using the constitutive and compatibility relations of the space suit.

The body of work that makes up this report includes experimentation, empirical and physics-based modeling, and model applications. A detailed space suit joint torque-angle database was compiled with a novel experimental approach that used space-suited human test subjects to generate realistic, multi-joint motions and an instrumented robot to measure the torques required to accomplish these motions in a space suit. Based on the experimental data, a mathematical model is developed to predict joint torque from the joint angle history. Two physics-based models of pressurized fabric cylinder bending are compared to experimental data, yielding design insights. The mathematical model is applied to EVA operations in an inverse kinematic analysis coupled to the space suit model to calculate the volume in which space-suited astronauts can work with their hands, demonstrating that operational human factors metrics can be predicted from fundamental space suit information.

2.0 Literature Review

The extravehicular mobility unit (EMU) space suit, which is currently used for NASA EVA's, has both hard fiberglass and soft fabric components. Mobility features, such as pleats that open as joints bend and rotational bearings, are built into all modern space suits. Without these mobility features, a person in a space suit would be virtually immobile. Even though space suits are designed to allow mobility, they restrict the wearer's motion in significant and complicated ways.[20]

Limited space suit joint torque-angle data has been reported in the literature. Studies that used human subjects wearing space suits reported higher torques than studies that measured torques on joints of empty, pressurized space suits. Higher torques with human subjects may be expected because contact between the space suit and the wearer's body affects the deformed shape of the space suit, but it is unclear whether the discrepancy in experimental results is due to shortcomings in experimental methods or actual differences in observed torques.[2, 7, 27, 28]

This research effort employed several mathematical and physical modeling techniques that were originally developed for other applications but are relevant to modeling an astronaut working in space, and specifically to provide an unique model of the torque-angle characteristics of space suit joints. Mathematical modeling techniques allow torques to be predicted from angle histories with accuracy, but, since they do not incorporate physical principles, they do not contribute insights for designing space suit joints with better mobility characteristics. Three mathematical techniques for modeling hysteretic systems, the Krasnoselski-Pokrovski model[21], the Preisach model,[26] and the Tao and Kokotovic model[35], which were originally used for modeling magnetization and shape memory alloy actuators, were evaluated for possible use. The Preisach model was chosen because it can produce output curves similar in shape to the space suit torque vs. angle curves and its identification process is relatively simple.

Physical models, in contrast to mathematical models, can lead to insights into the physical processes that govern space suit mobility. Two physical models of the bending characteristics of inflated cylinders may be relevant to space suit joints. The beam model treats the inflated cylinder as a beam with a fabric wall that stretches, maintaining a constant internal volume. The mobility of the space suit joint is determined by elastic behavior of the fabric wall.[22-25] The membrane model treats the fabric shell as an inextensible membrane. Bending deflections of the cylinder result in shape and volume changes. The work required to bend the joint is entirely due to compression of the gas inside the tube [9,10] Differences in torque predictions between the beam model and the membrane model illustrate the relative importance of elasticity and gas compression in space suit joint mobility.

One application of space suit joint mobility models is in calculating human factors performance metrics, including the one-handed space suited work envelope, which indicates the volume within which a space-suited astronaut can comfortably work with one hand. The current NASA space-suited work envelope[1], which is used in planning EVA's, differs qualitatively from other work envelopes found in the literature.[29] A recently-developed computational technique allows suited work envelopes to be calculated using mathematical models of the torque-angle characteristics and kinematics of a space suit.[19, 15-18]

3.0 Space suit mobility database

3.1 Experiment overview

The objective of the experimental portion of this research effort was to obtain a quantitative database of joint angles and torques required to move a space suit's joints, under realistic conditions. The impossibility of directly measuring joint torques in suited humans necessitated an indirect measurement approach, using both human subjects and an instrumented robot to obtain torque data.

The human test subjects carried out arm and leg motions both wearing the space suit and not wearing the space suit, supplying realistic joint angle trajectories for each of 20 motions. The joint angle trajectories produced by the human subjects were then used as command inputs for the robot, so that the robot imitated the humans' motions while torques were measured at each of the robot's joints. Torques on the robot's joints due to the weight of the robot and space suit, were subtracted, resulting in a consistent set of joint angle and torque data.

3.2 Space suit description

The space suit used in these experiments was an Extravehicular Mobility Unit (EMU) supplied under contract by Hamilton Sundstrand. A size large hard upper torso (HUT) was used.The space suit that was tested was as close as feasibly possible to a space suit that would be used in flight, however there were some differences between this space suit and a flight-qualified space suit. The space suit tested was designated as Class III hardware, approved for demonstrations or non-hazardous testing. Class III space suits are known to be less stiff than Class I, or flight qualified suits, because they are generally older and have been used more. Additionally, the scye bearings on the space suit used in these experiments, which connect the arms to the HUT, were mounted on a single-fold bellows, which allows some additional shoulder range of motion. This bellows configuration, known as a pivoted HUT, is no longer used in flight.

Life support for the suited test subjects was provided by supplying breathing air on a non-recirculating vent loop. Air was supplied to the suit inlet by scuba tanks and exhausted from the suit to maintain a minimum air flow rate. One set of scuba tanks lasted approximately one hour. A volumetric mock-up was substituted for the portable life support system (PLSS), resulting in an overall weight for the space suit and PLSS mock-up of 102 lb. (46.4 kg). In all cases, the space suit was pressurized to 4.3 psi (30 kPa) above ambient pressure.

3.3 Data collection with human subjects

Subjects Four male subjects participated in the experiment; two of the subjects were experienced in 1-g testing of the EMU. Subjects performed arm and leg motions in two sessions. The first session was conducted without the space suit and the second session was performed with subjects wearing the space suit, one week later. One of the inexperienced test subjects did not conduct the simple motions described in Section for space-suited data collection because of a scheduling constraint. The experiment was approved by MIT's Committee on the Use of Humans as Experimental Subjects and informed consent was obtained from each subject prior to each experimental session.

Motions Human test subjects carried out arm and leg motions while wearing the space suit. Twenty motions were used for human and robot data collection. The motions, listed in Table 1, included 11 simple motions that isolated each of the robot's degrees of freedom (wrist rotation was not used) and 9 complex, free-form motions, which included reaching over the head, across the body and to an object 50 cm above the floor. Subjects also walked on a treadmill and traversed a 12 cm high step to simulate planetary EVA tasks. Trial ordering was randomized, with a first phase of simple motions followed by a second phase of complex motions. Subjects were instructed to move through the maximum range that they could comfortably reach. They were not instructed to attempt to achieve the maximum range of motion. Free-form motions were included for two reasons: to obtain data on multi-joint, non-planar motions and to compare the subjects' choices of arm and leg positions between suited and unsuited conditions.

TABLE 1. Arm and leg motions used in experiment

Simple Motions	Complex Motions
Shoulder flexion	Arm swing forward-backward
Shoulder abduction	Arm swing side to side
Humerus rotation	Leg swing forward backward
Elbow flexion	Leg swing side to side
Hip flexion	Overhead reach
Hip abduction	Cross-body reach
Thigh rotation	Low reach
Knee flexion	Locomotion over 12 cm step
Ankle rotation	Locomotion on treadmill
Ankle flexion	
Ankle inversion	

Figure 1 shows an example of a subject performing the low reach trial. In the low reach trial, the subject's task is to reach down and to the left, touching the corner of the step with his right hand.

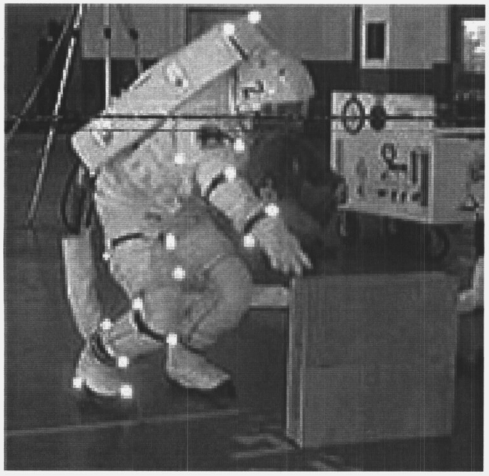

FIGURE 1. Low reach trial.

Data acquisition Kinematic data was collected on the subjects' right arm and leg, using a Multitrax optical motion capture system (Adaptive Optics Associates, Cambridge, MA). Reflective markers were placed on the subject's right arm, right leg and the mock-up PLSS, as shown in Figure . Outputs from the motion capture system were x, y, and z positions of each of the markers in a laboratory-based coordinate system. Marker positions for suited and unsuited configurations are shown in Figure .2

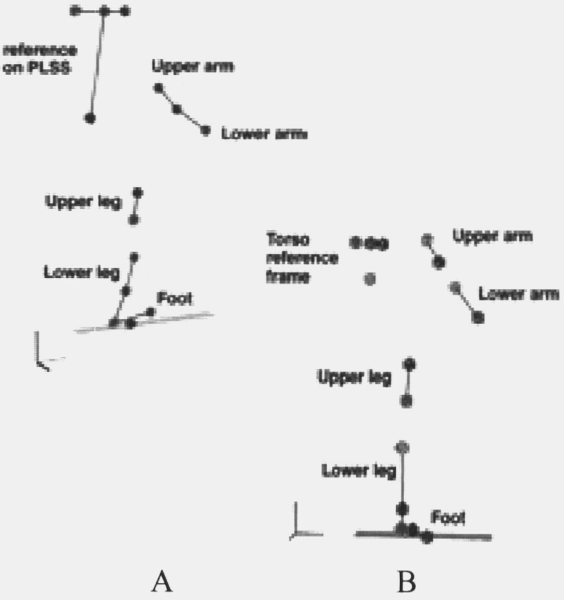

FIGURE 2. Marker configurations for A.) suited and B.) unsuited configuration.

The Cartesian positions of the markers were converted into joint angles for 11 arm and leg joints, which completely describe the kinematics of the right arm, leg, and foot. Joint angles are measured with respect to the body segment closer to the torso or with respect to the torso in the case of the shoulder and hip joints. When all joint angles are zero, the arm and leg are both parallel to the torso and the palm of the hand and the toe both point forward. Each of the joint angles, with its zero position and positive direction, are shown in Figure 3. Figure A shows the five flexion angles: shoulder flexion (sf), elbow flexion (ef), hip flexion (hf), knee flexion (kf), and ankle flexion (af). Figure B shows shoulder abduction (sa), hip abduction (ha), and ankle inversion (ai). Figure C illustrates the thigh rotation angle (tr), when hf=90 degrees and kf=90 degrees. Figure D and Figure E are both overhead views, showing, in Figure D, the humerus rotation angle (hr), with ef=90 degrees, and in Figure E, the ankle rotation angle.

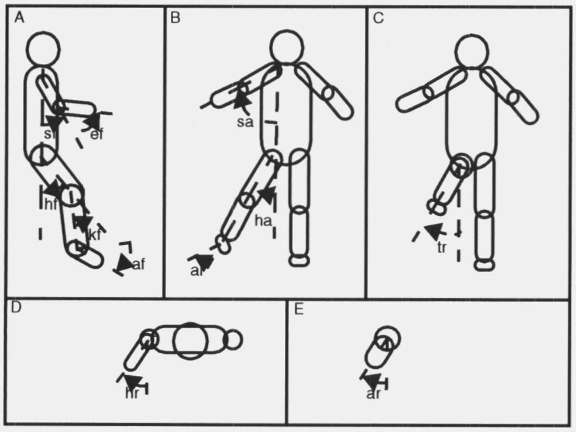

FIGURE 3. Joint angle conventions used for kinematic data for human test subjects and robot.

3.4 Robot data collection

Robotic Space Suit Tester, or M. Tallchief

Known in our lab as M. Tallchief, a robotic space suit tester was built by Sarcos, Inc. (Salt Lake City, UT) for space suit mobility testing under the Small Business Innovative Research (SBIR) program for NASA Johnson Space Center. The robot, or M. Tallchief, was loaned to MIT by NASA in 1998 for space suit mobility research.

M. Tallchief has 12 hydraulically actuated joints on the right arm and leg and 12 posable joints on the left arm and leg. At each actuated joint, potentiometers measure joint deflection and strain gauge load cells measure torque. Locations of the robot's joints are indicated in Figure 4 and Table 2.

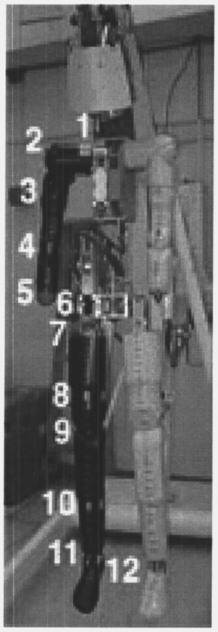

FIGURE 4. The 12 degrees-of-freedom of M. Tallchief's joints.

TABLE 2. RSST joint degrees of freedom

Number	Joint
1	shoulder flexion
2	shoulder abduction
3	humerus rotation
4	elbow flexion
5	wrist rotation
6	hip flexion
7	hip abduction
8	thigh rotation
9	knee flexion
10	ankle rotation
11	ankle flexion
12	ankle inversion

The robot is suspended from a crane and supported at two points: a bolt at the "head" and a cable attached to the back, near the center of the torso. The torso is considered to be the ground segment and remains in a fixed position, while the arm and leg move with respect to the torso. Adjustment of the cable supporting the torso allows the robot's pitch angle to be adjusted and two positioning joints within the torso allow forward/backward and left/right bending of the torso segment.

The actuated joints of the robot are powered by an MTS model 510 hydraulic pump. Hydraulic fluid circulates in a loop from the pump, through each robot joint actuator, then back to the pump. All of the hydraulic lines and electrical cables exit the robot through a seal at the top so that a space suit may be pressurized on the robot.

Control of robot motions is accomplished through analog circuitry and two PC computers, as shown in Figure 5. An EPC-5 486 computer supplies the user interface, and an EPC-6 386 computer performs the lower-level control functions. Analog control loops are closed on position, velocity, and torque on circuit boards in the Advanced Joint Controller (AJC) cage, with control gains supplied by the EPC-6 through a digital interface. The AJC cage uses a modular architecture, with 12 boards, one for each joint. The EPC-5 computer runs a Microsoft Windows 3.1 based user interface, called the Robotic Space Suit Tester Application (RSSTA), which passes commands to the robot at an update rate of 5 Hz and records position and torque data to disk. At the time the robot was built, the analog/digital command and control architecture allowed for faster loop closure than would have been possible by closing control loops in the digital domain in a computer. Although the analog position, velocity, and torque servo loops are hard-wired on the circuit boards, the computer interface does allow for time-varying control gains, a capability which has not been implemented in this study.

The combination analog-digital control system is very robust to computer crashes, which happen periodically in Windows 3.1. If the EPC-6 computer stops receiving inputs from the EPC-5 computer, it holds the current commands to the robot's joints. All of the control loops remain closed, so stability and performance of the robot's control system are preserved when the EPC-5 computer crashes. In addition, the modular construction of the analog circuitry in the AJC cage aids in troubleshooting. Boards for different joints may be exchanged for diagnostic purposes by changing jumper settings and inserting the boards in different slots in the AJC cage.

The user interface program allows the robot to be commanded in two ways: joints can be manually positioned by clicking on arrows in the positioning window or multi-joint trajectories can be loaded from files and executed. Joint positions and torques, sampled at 5 Hz, can be plotted on the screen and saved to files. Trajectories for the robot to follow may be created interactively, by manually positioning the robot and saving a series of trajectory points. The list of robot positions can be saved as a file and run at user-set speeds. Trajectories can also be created outside of the RSSTA application.

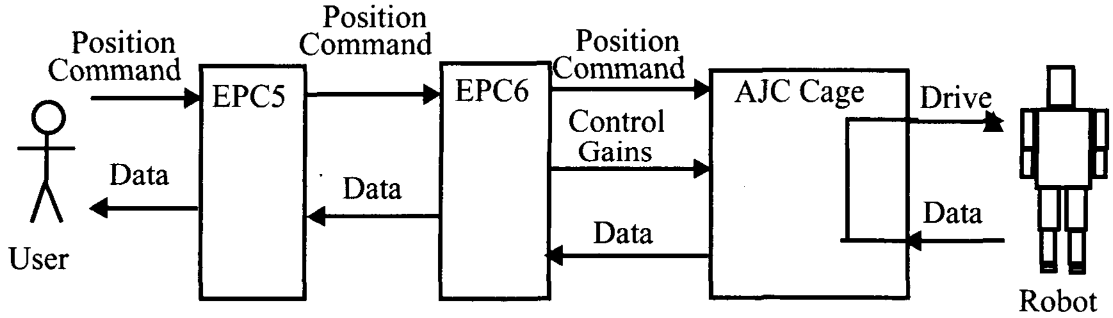

FIGURE 5. RSST command and control.

Robot operations

Trajectory generation

M. Tallchief was designed to approximate the joint axes and range of motion of a human arm and leg, but due to geometrical constraints in its construction, the robot has less range of motion in some joints than humans do. In particular, limits on two of the shoulder degrees of freedom and one of the hip joints are quite different from those of human joints. The shoulder flexion joint does not allow negative shoulder flexion angles, which bring the arm past vertical, behind the body. The shoulder abduction joint also does not allow negative shoulder abduction angles, which bring the arm towards the body. Like the shoulder flexion joint, the hip flexion joint does not allow the hip to be flexed beyond vertical, behind the body. A complete list of the robot's range of motion for each joint is given in Table 3, using the joint angle definitions from Figure .6

The robot's limited range of motion prevents the raw kinematic data files collected from the human test subjects from being used directly to command the robot.

Commanding the robot with a joint angle that is beyond its range causes the joint to move to its limit and abruptly stop. To avoid spurious torque data caused by sudden changes in robot joint velocity, the data files collected from the human subjects were pre-processed so that all of the commanded joint angles were within the robot's range of motion.

TABLE 3. Robot joint angle limits

Joint	Maximum angle (deg)	Minimum angle (deg)
Shoulder flexion	180	-15
Shoulder abduction	90	0
Humerus rotation	90	-90
Elbow flexion	130	0
Hip abduction	45	0
Hip flexion	100	0
Thigh rotation	22	-22
Knee flexion	130	0
Ankle rotation	20	-20
Ankle flexion	30	-45
Ankle inversion/eversion	20	-20

There are several methods that may be used to force commands to the robot to stay within the robot's limits. The simplest method is to uniformly reduce the amplitude of the entire joint trajectory so that the maximum displacement falls within the limits. The problem with this approach is that it modifies the joint angle values for the entire data file, even though the vast majority of joint angle values are permissible. A more complicated scheme that minimizes changes to valid joint angles and discontinuous velocities while forcing the output joint angle trajectory to remain within the robot's limits was implemented instead.

A nonlinear scaling method was used to eliminate robot joint commands that are outside the limits, while leaving non-extreme trajectory angles unchanged. This scheme forces the robot's commands to be in bounds by compressing the out-of-bounds angle values into a region near, but inside of, the joint angle limits. Compressing the out-of-bounds data rather than deleting it reduces velocity discontinuities, which may cause erroneous torque measurements.

The pre-processing scheme takes a desired robot command, $x(t)$, as an input, multiplies it by a scaling factor $f(t)$, and outputs $y(t)$, the modified command, which does not exceed the robot's limits for that joint. Two robot joint limit values were defined, as shown in Figure : b is the maximum possible robot joint displacement, and a is 90% of the way from the midpoint of the robot's joint range to b. Values of the input, $x(t)$, which exceed b are reduced to fall between a and b, while input values which are less than a are not changed. The maximum value of the input, $x(t)$, is called x_m. A scaling factor $f(t)$ that accomplishes this transformation is given in Equation 1, where k and c are constants whose values are set by matching boundary conditions.

$$
\begin{aligned}
x(t) < a \qquad & f(t) = 1 \\
x(t) > a \qquad & f(t) = \frac{1}{1 + k\frac{(x-c)}{b}}
\end{aligned}
\qquad \text{Eq 1}
$$

The constants k and c are set so that at $x=a$, $y=x$ and at $x=x_m$, $y = b$. The $f(t)$ that satisfies these conditions is given by Equation 2.

$$
\begin{aligned}
& & y(t) &= f(t)x(t) \\
& x(t) < a & f(t) &= 1 \\
x(t) > a & & f(t) &= \frac{1}{1 + \frac{(x_m - b)}{(x_m - a)} \frac{(x(t) - a)}{b}}
\end{aligned}
\qquad \text{Eq 2}
$$

The results of applying this transformation are shown in Figure 6. For $0<t<t_1$, the input value, x, is less than a. The corresponding $f(0<t<t_1)$ is equal to 1 and consequently, the output $y(0<t<t_1)=x(0<t<t_1)$. When x is greater than a, for $t_1<t<t_2$, f is less than 1, and reaches a minimum of $f=b/x_m$ when x is at its maximum of x_m. Thus, the maximum output value is equal to b, the maximum allowable command. The plot of $y(t)$ vs. t illustrates that y is always less than b and y is equal to the input value, x, when x is less than a.

Equation 2 is valid only for non-zero, positive a and b. For negative or zero a and b, the same transformation can be accomplished by mirroring $x(t)$ about the joint range midpoint, m, using Equation 3 to obtain $x'(t)$. The mirrored input $x'(t)$ is then transformed according to Equation 2, and the output, $y'(t)$ is then mirrored back according to Equation 3.

$$x' = 2m - x \qquad y = 2m - y' \qquad \text{Eq 3}$$

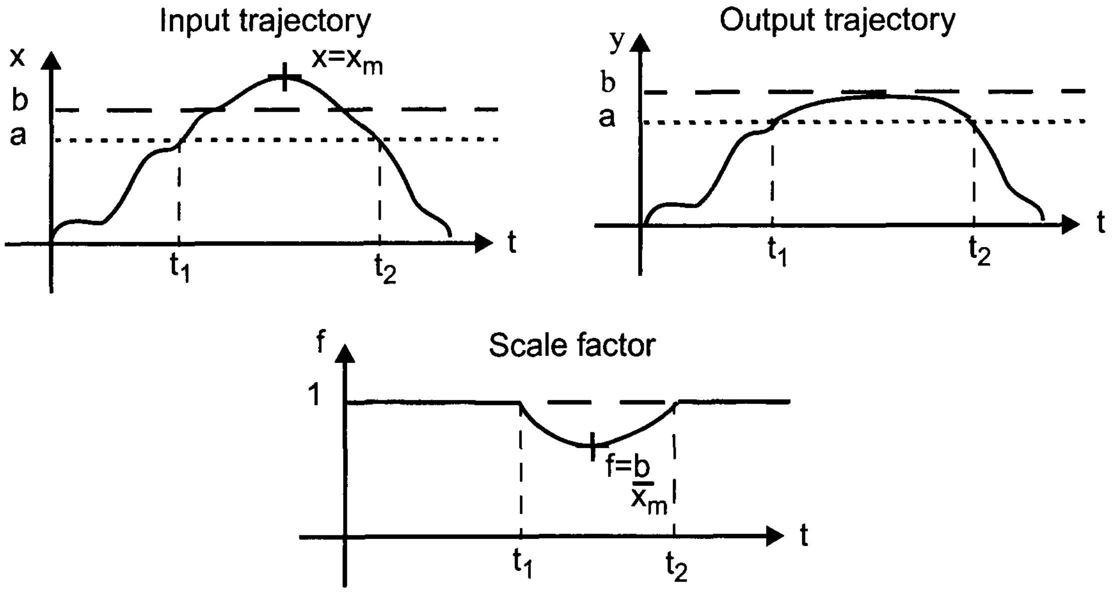

FIGURE 6. Trajectory motion limiting algorithm.

The pre-processed commands for the robot are then formatted into trajectory files that the RSSTA application can read. The robot's trajectory files are ascii text files, which are normally created in the RSSTA application when the user manually positions the robot and saves trajectory points. Trajectory files were created from pre-processed data with the Matlab script trajconvert.m, which emulated the file format of the trajectory files created in RSSTA. Each trajectory file begins with three lines of text. Each line ends in a line feed character (ctrl-j or ascii 10). Following the three text lines are the commanded joint positions. Each line contains joint positions for the 12 joints, with up to 3 digits before the decimal point and 1 digit after it. Numerical values are aligned horizontally on decimal points. Numbers are separated by spaces so that there are always 6 characters between each successive decimal point, 4 characters before the first decimal point in the line, and 2 characters after the last decimal point. Every line ends in a line feed (ctrl-j or ascii 10) and the end of file character is a carriage return (ctrl-m or ascii 13). If a trajectory file deviates from this format, either the RSSTA application will hang or it will load a short trajectory with incorrect joint angle values.

Trajectory speed setting

The speed at which the robot moves through a trajectory is set by the operator in RSSTA at the time the trajectory is executed, which allows the same trajectory to be run at various speeds. Speed setting is accomplished by entering a single velocity value in degrees per second, between 1 deg/sec and 50 deg/sec. The operator-entered velocity is assigned to the maximum velocity of the robot joint that has the largest angle range in that trajectory. For this experiment, the robot should move through the trajectory at the same speed as the human subject did. In order to accomplish this, the joint with the maximum range and its maximum velocity would have to be determined beforehand, stored, and correctly entered by the robot operator each time the trajectory is run.

In order to reduce the likelihood of errors, a different method was used to set trajectory speeds. The wrist rotation joint mechanism had been removed from the robot, to allow the robot's arm to fit in the EMU sleeve, as described in Section . A dummy command to the wrist rotation joint is included in all trajectory files for motion from -90 degrees to +90 degrees at a constant velocity of 50 deg/sec. The wrist rotation joint then has the maximum range and its velocity is set by the operator's speed input. To run trajectories at the same speed as the human subjects moved, the operator enters 50 deg/sec for all trajectories.

Torque limits

Torque limits for each joint are set and enforced by the RSSTA software. When a motion trajectory is running and one or more of the joint torques exceed the limits, the robot's motion stops and the robot is commanded to return to the starting position of that trajectory. A dialog box is displayed indicating the joint that triggered the torque limit violation. Only one dialog box appears, even if multiple torque violations occur. Torque limits are not checked in manual operation. The joint torque limits used in the experiment are listed in Table 4. The limits used for wrist rotation are necessary because the wrist rotation load cell is disconnected and the open circuit returns a constant value of -819 in*lb for wrist rotation torque.

TABLE 4. Robot torque limits

Joint	Minimum Torque (in*lb)	Minimum Torque (Nm)	Maximum Torque (in*lb)	Maximum Torque (Nm)
Shoulder flexion	-400	-45.2	350	39.6
Shoulder abduction	-400	-45.2	350	39.6
Humerus rotation	-250	-28.3	250	28.3
Elbow flexion	-350	-39.6	275	31.0
Wrist rotation	-900	-102	500	56.5
Hip abduction	-400	-45.2	2000	226
Hip flexion	-1300	-147	1300	147
Thigh rotation	-500	-56.5	500	56.5
Knee flexion	-750	-84.8	750	84.8
Ankle rotation	-500	-56.5	500	56.5
Ankle flexion	-700	-79.1	700	79.1
Ankle inversion/ eversion	-500	-56.5	500	56.5

Space suit installation

Although the robot had been designed for space suit mobility research, a space suit had never previously been installed. Several modifications were made to the robot to allow the EMU to fit properly and protect the space suit from damage. These included replacement of structural parts in the robot and removal of non-essential assemblies for ease in installing the space suit.

The structural component between the top of the robot's torso and the electrical-hydraulic feed through interface, referred to as the neck, was replaced to allow a gas-tight interface with the EMU space suit. The new neck has an angle of 25 degrees between its top and bottom surfaces, replacing the original neck which has a 55 degree angle between its top and bottom, as shown in Figure 7.

The neck piece provides the mechanical interface between the EMU and the robot. When the space suit is installed on the robot, an aluminum plate, called the neck plug, is mounted to the neck ring of the HUT, where the helmet attaches. The aluminum plate is bolted to the robot's neck piece, so that the space suit is supported by the neck ring, rather than the inner surface of the HUT at the shoulders. The neck plug has a hole in the center for hydraulic hoses and electrical cables to pass through. Sealing is accomplished with an airtight seal between the EMU neck ring and the neck plug and a rubber gasket between the neck plug and the robot's feed through interface, which is bolted directly above the neck plug.

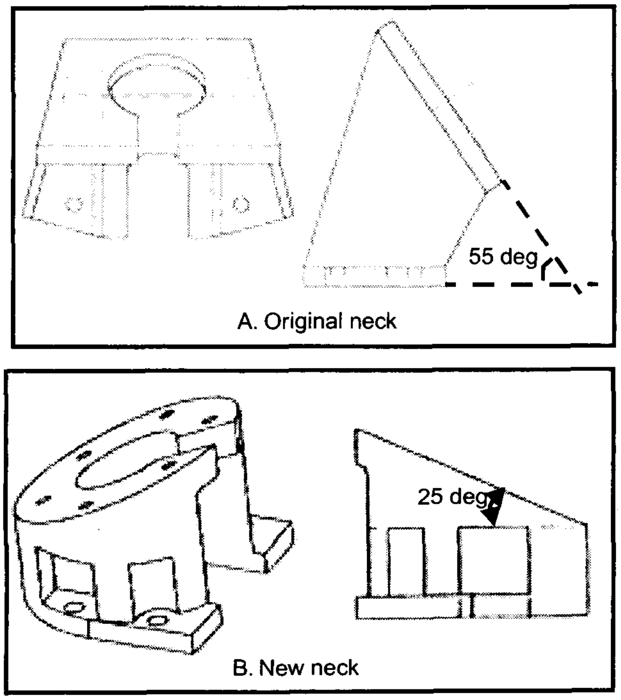

FIGURE 7. A.) Original neck with angle of 55 degrees. B.) New neck with angle of 25 degrees.

In its original configuration, the robot's torso was approximately 2.5 cm too long to allow the HUT and lower torso assembly (LTA) of the space suit to connect. The torso of the robot was shortened by replacing a torso structure piece with a piece that was 3.2 cm shorter. The location of the modified torso piece is shown in Figure 8. A screw at the bottom of the robot's torso was also replaced with a low-head version, to further shorten the torso.

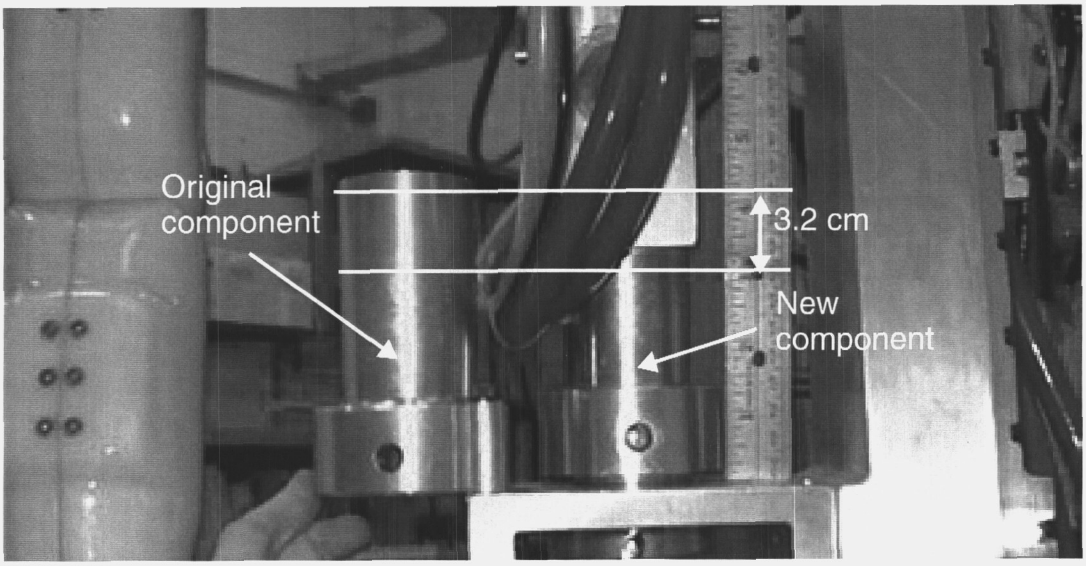

FIGURE 8. Modified torso structure piece, with original, larger torso structure piece at left.

The robot's lower arm also did not fit inside the space suit. The wrist rotation shaft and wrist disk were removed, shortening the lower arm length by 8.9 cm and reducing the arm end diameter from 7.6 to 6.4 cm. As a result, the wrist rotation joint was not functional, but it was never intended to be used in the experiment.

In order to ease installation of the space suit on the robot, and eliminate the need to accurately size both arms and legs of the space suit, the robot's non-actuated left arm was removed at the shoulder flexion pivot. The left foot was also removed at the ankle inversion pivot.

To protect the space suit from sharp edges and pinch points on the robot, a wet suit was placed on the robot before the space suit was installed. Foam padding was also used at the lower end of the plastic shell on the lower leg to prevent the space suit's bladder material from being pinched between the foot shell and the lower leg during ankle flexion motion. A plastic cover was placed over the exposed end of the wrist rotation shaft.

To install the space suit on the robot, the hydraulic lines and electrical cables were disconnected and the robot was disconnected from the crane. The robot's feed through interface was then removed, down to the neck piece. With the robot held in a sitting position on the floor, the HUT was first installed on the robot. The arm was brought above the head and the shoulder latch was released by inserting an allen wrench through the access hole in the shell and pushing the latch mechanism, as shown in Figure 9. When the shoulder latch is released, the upper portion of the arm, which is normally horizontal, can be rotated to a vertical position so that the arm can be brought through the sleeve of the HUT. Care should be taken to ensure that the shoulder latch is engaged properly following installation of the HUT. The HUT was attached to the robot by bolts that pass through the robot's feed through interface and the space suit's neck plug into the robot's neck piece. Using small lengths of threaded rod to align the bolt holes while the three parts are assembled aids this process. The robot was then reconnected to the crane, hydraulic lines, and electrical cables and raised to its normal position. The LTA, with the right boot removed, was pulled up over the legs and latched to the HUT at the body seal closure and the right boot was replaced.

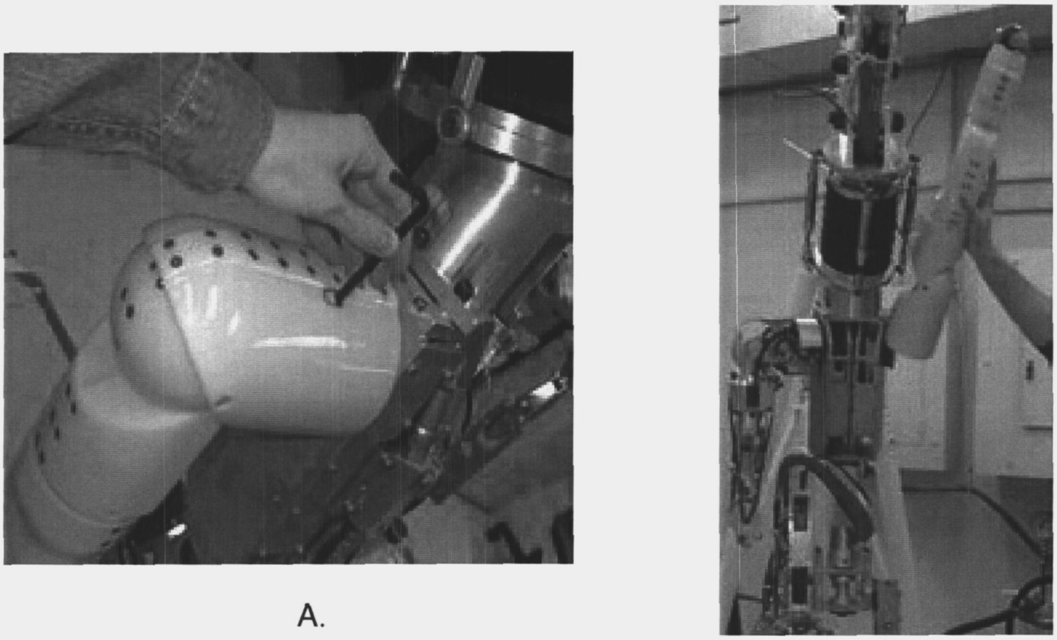

A.

B.

FIGURE 9. Shoulder latches. A.) Latch location. B.) Arm position with latch released.

Position and torque data collection

The EMU used in the human subjects phase of the experiment was installed on the robot and pressurized to 30 kPa (4.3 psi), as shown in Figure 10. Air was supplied from a scuba tank to maintain the 30 kPa (4.3 psi) operating pressure in the space suit. Due to a high leakage rate in the robot-space suit interface, one scuba tank lasted approximately 30 minutes. The high leakage rate required a suit depressurization and repressurization to replace the air tank every 30 minutes while data was being collected.

FIGURE 10. EMU installed on robot.

The space-suited robot performed 80 different motions that had been generated by the human test subjects. Robot joint angle and torque data for the 11 robot joints was obtained at both the speed that the human test subjects performed the motions and at half speed, to improve the robot's trajectory-following performance. A total of 247 torque-angle data sets were obtained from the suited robot, including several replications of each motion. In addition to the robot-generated angle and torque data, motion capture data was acquired for at least one replication of each motion, using the Adaptive Optics Associates optical motion capture system that had been used for data collection with human subjects.

The robot also performed the above-listed motions without the space suit under two conditions: wearing the wet suit that had been used in space-suited data collection to protect the space suit from sharp edges on the robot and not wearing the wet suit. The unsuited torque and angle data was collected at full speed and half speed, the same speeds at which the suited data had been collected. Over 300 torque-angle data sets were collected from the robot without the space suit. Figure 11 shows in schematic form the nine motion capture and robot-generated data files that originate from one motion of the space-suited human subject. This report presents the space-suited human motion capture data and the robot-generated torque and angle data under suited and unsuited conditions.

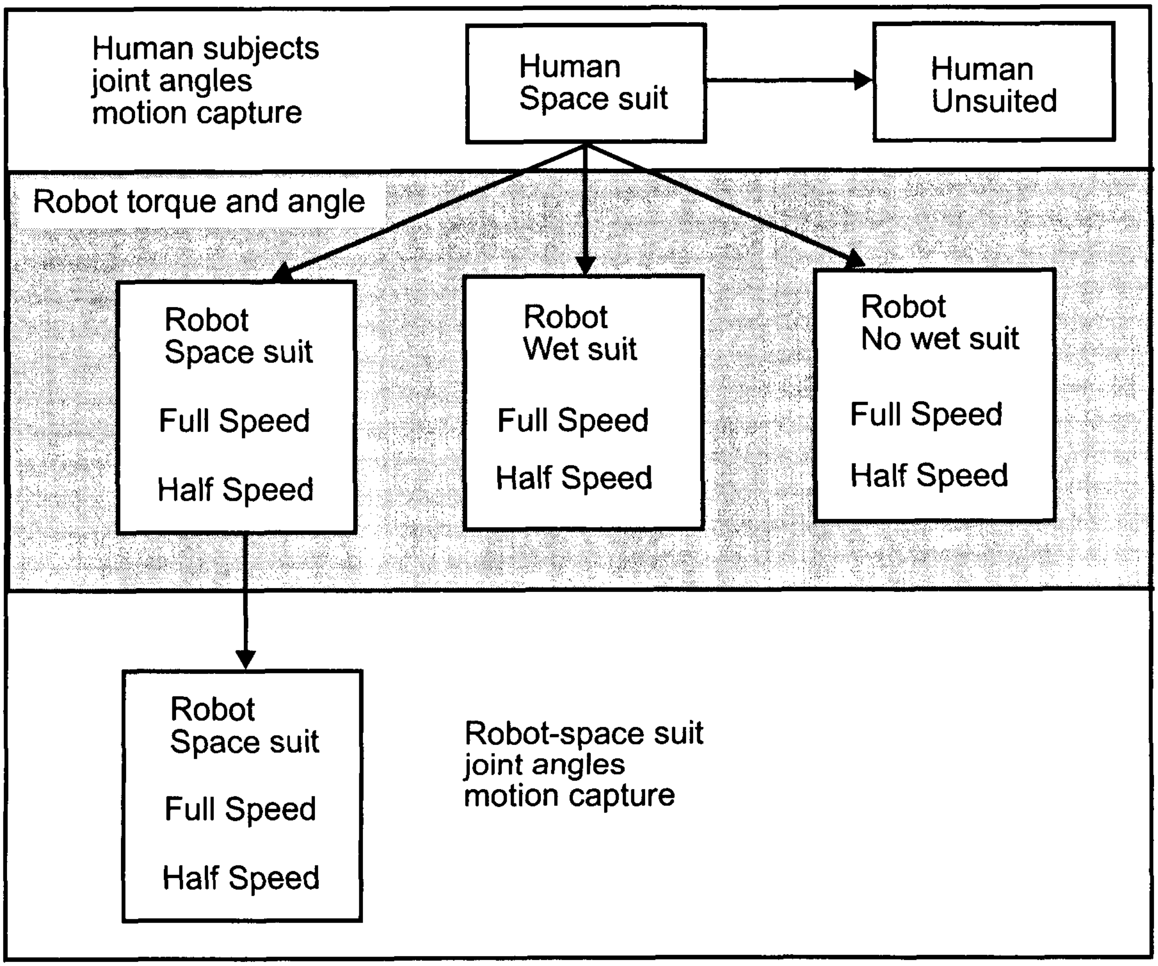

FIGURE 11. Schematic of data collected from human subjects and robot.

3.5 Data reduction

The torque data that was recorded by the robot is a composite of torques required to support the weight of the robot's limb, support the weight of the space suit arm or leg, and bend the joints of the space suit. Only the torques required to bend the space suit's joints are relevant to the space suit model. Both experimental data and kinematic analysis were used to calculate the gravity-induced torques due to the robot and space suit. The gravity-induced torques were then subtracted from the joint torques recorded by the robot.

Robot weight removal

An empirical method was chosen for estimating torques induced by the robot's weight because the robot's mass properties are not documented. Torques caused by the robot's weight were measured by recording torque data while the robot performed all of the same motions that were used in suited robot data collection. The torques caused by the robot's weight were eliminated from the measured torque data by manually aligning the two files in time and subtracting the unsuited torque data from the suited torque data. Data collected with the robot wearing the wet suit only was used as the unsuited torque data. All data presented here has been corrected to remove torques induced by the weight of the space suit and robot.

Space suit weight removal

Torques caused by the space suit's weight were estimated using kinematic analysis techniques, based on both the known mass properties of the space suit and the robot dimensions and joint axes. The kinematic analysis yielded the positions and orientation of each of the robot and space suit segments. Joint torques were calculated based the relative positions of the space suit segment centers of mass and the robot joints.

The geometry of the torque calculation is shown in Figure 12. The vector from joint i to the center of mass of segment j is $\underline{r}_{ij}$, $\underline{z}_i$ is the axis of joint i, m_j is the mass of segment j, and g is the acceleration due to gravity. The torque caused by the weight of segment j about a point on $\underline{z}_i$ is given by:

$$\underline{T} = \underline{r}_{ij} \times m_j \underline{g} \quad . \qquad \text{Eq 4}$$

Only the torque along $\underline{z}_i$ is measured by the robot's load cell at that joint, so the torque measured by the load cell on joint i is given by Equation 5.

$$T_{ij} = (\underline{r}_{ij} \times m_j \underline{g}) \bullet \underline{z}_i \qquad \text{Eq 5}$$

The torque on each joint due to the suit weight is the sum of the T_{ij} torques for each segment that is further away from the torso than joint i is.

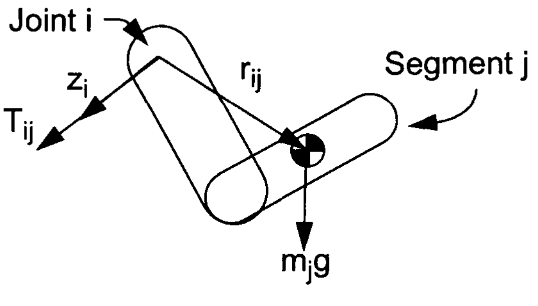

FIGURE 12. Gravity-induced torque T_{ij} of segment j on joint i.

Using the Denavit-Hartenburg notation for robot kinematics, the position, $\underline{r}_i$, and orientation, $\underline{z}_i$, of each of the robot's joints and the position of the center of mass of each space suit segment, $\underline{r}_j$, were calculated, giving the $\underline{z}_i$ and $\underline{r}_{ij}$ vectors for a given set of joint angles. Coordinate axes used on each of the robot's arm and leg segments are shown in Figure 13. The Denavit-Hartenburg notation prescribes the locations of the x and z axes, based on the joint axes of the current segment and the previous segment.[5, 14] The y axes are chosen to form a right-handed set of coordinates.

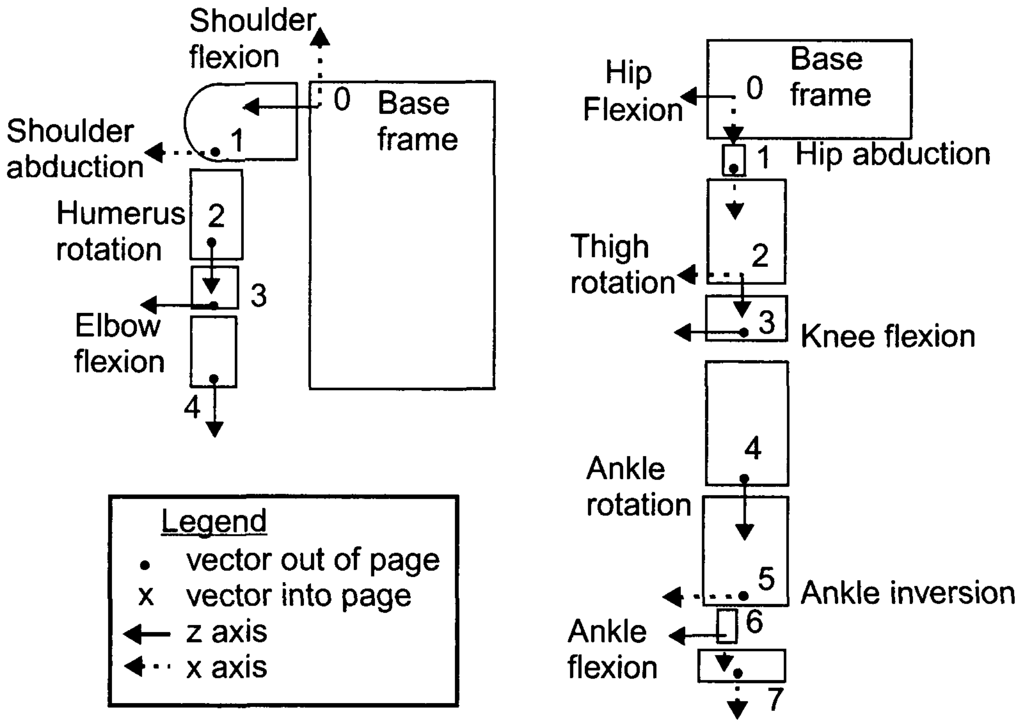

FIGURE 13. Coordinate axes for robot's arm and leg.

Based on the coordinate axes shown in Figure 13 and the joint angle definitions from Figure 3, the four Denavit-Hartenberg link parameters, *a*, *d*, α, and θ, for each robot segment are given in Table 5 for the leg and Table 6 for the arm.

TABLE 5. Leg link parameters

Link number	a (m)	d (m)	α (deg)	θ(deg)
1	0.0699	0	-90	hf
2	0	0	-90	-ha-90
3	0	0.40	-90	tr-90
4	0	0	90	kf
5	0	0.43	90	ar+90
6	0.0338	0.0157	90	ai+90
7	0.0845	0	-90	af
8	0	0.220	0	0

TABLE 6. Arm link parameters

Link number	a (m)	d (m)	α (deg)	θ (deg)
1	0	0.127	90	sf
2	0	0	-90	-sa+90
3	0	0.318	-90	-hr-90
4	0.140	0	90	ef-90

The position and orientation of each segment are represented by 4x4 homogeneous matrices. The homogeneous matrix that transforms coordinate frame *i-1* to coordinate frame *i* with rotation *R* and translation by vector $\underline{x}$ is given by:

$$A_{(i-1)i} = \begin{bmatrix} R & x \\ 0\ 0\ 0 & 1 \end{bmatrix} = \begin{bmatrix} \cos\theta_i & -\cos\alpha_i \sin\theta_i & \sin\alpha_i \sin\theta_i & a_i \cos\theta_i \\ \sin\theta_i & \cos\alpha_i \cos\theta_i & -\sin\alpha_i \cos\theta_i & a_i \sin\theta_i \\ 0 & \sin\alpha_i & \cos\alpha_i & d_i \\ 0 & 0 & 0 & 1 \end{bmatrix}$$

Positions and orientations are propagated down the kinematic chain by multiplying the $A_{i,\ i+1}$ matrices. The homogeneous matrix representing the transformation from the base coordinate frame to the frame of segment *n* is given by Equation 6:

$$T_{0n} = \prod_{1}^{n} A_{(i-1)i} \qquad \text{Eq 6}$$

By multiplying the $A_{i,\ i+1}$ matrices corresponding to each segment, the position and orientation of each of the robot's joints can be calculated. Positions of space suit segments are calculated by considering each space suit segment to be a shorter version of one of the robot's segments, with a length equal to the distance from the next robot joint closer to the torso to the space suit segment center of mass. To calculate a space suit center of mass position, the space suit segment is used as the terminal segment of the chain. Link parameters and masses of the space suit segments are given in Table 7.

TABLE 7. Space suit link parameters

Space suit link	Corresponding robot link	*a*(m)	*d*(m)	*a*(deg)	*q*(deg)	mass (kg)
upper arm	3	0	0.225	-90	-hr-90	0.677
lower arm and glove	4	0.196	0	90	ef-90	2.25
upper leg	3	0	0.239	-90	tr-90	0.741
lower leg	5	0	0.252	90	ar+90	1.18
boot	8	0	0.0668	0	0	2.24

For each time step in the robot suited data file, the robot joint angle data is used to calculate the $A_{i,\ i+1}$ matrix for each robot and space suit segment. The $A_{i,\ i+1}$ matrices are multiplied to obtain the $\underline{r}_i$ vectors that go from the origin of the base coordinate frame to the origin of the segment *i* coordinate frame, the $\underline{z}_i$ vectors that indicate the axis orientation of joint *i*, and the $\underline{r}_j$ vectors that go from the origin of the base coordinate frame to the center of mass of space suit segment *j*. The robot and space suit link position and orientation vectors are substituted into Equation 5 to obtain the torque caused by the weight of space suit segment *j* on joint *i*. The space suit weight-induced torques are then summed for each joint to obtain the torque caused by the space suit's weight. Torques due to the space suit's weight are then subtracted from the robot's torque data.

3.6 Experimental Results

Example data

After both the robot's weight and the space suit's weight are eliminated from the recorded torque data, the remaining torques indicate the torque necessary to bend the joints of the space suit. Examples of the space suit-induced torque plotted vs. joint angles are shown in Figure 14 - Figure 18. Each of the example plots represents one test subject and one experimental trial, which includes several repetitions of the motion. Joint angles are measured according to the definitions provided in Figure 3.

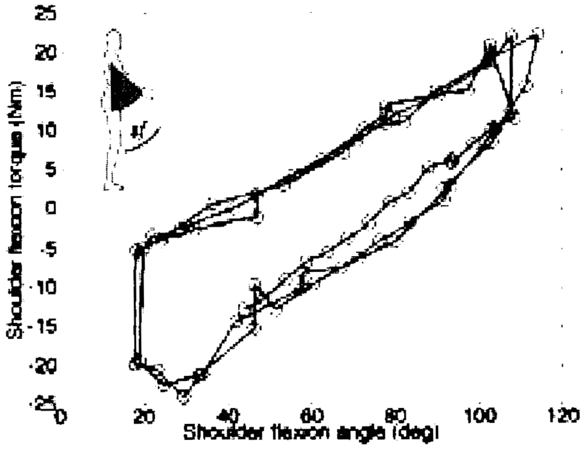

FIGURE 14. Shoulder flexion torque vs. angle, 3 repetitions.

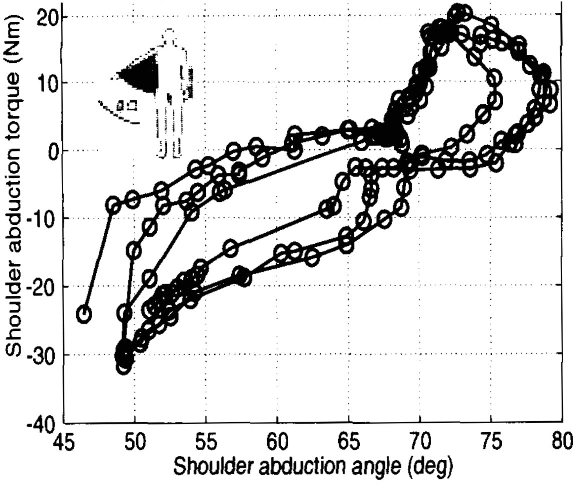

FIGURE 15. Shoulder abduction torque vs. angle, 3 repetitions.

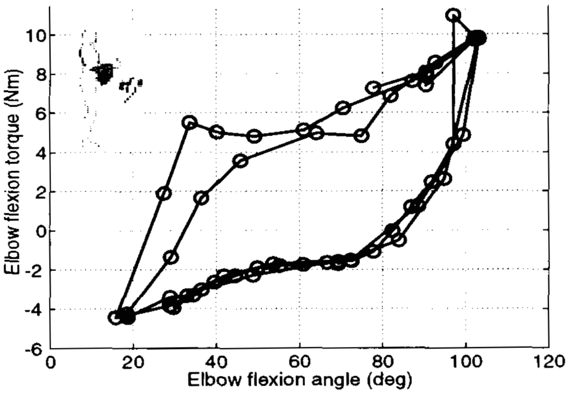

FIGURE 16. Elbow flexion torque vs. angle, 2.5 repetitions.

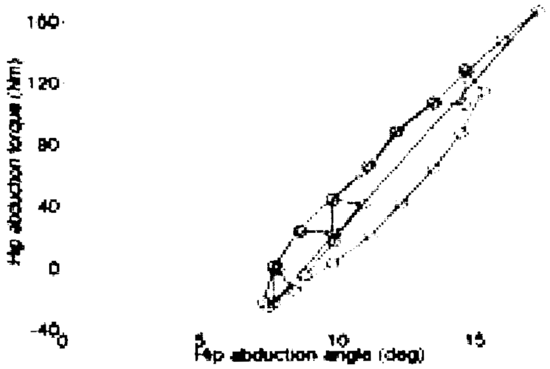

FIGURE 17. Hip abduction torque vs. angle, 3 repetitions.

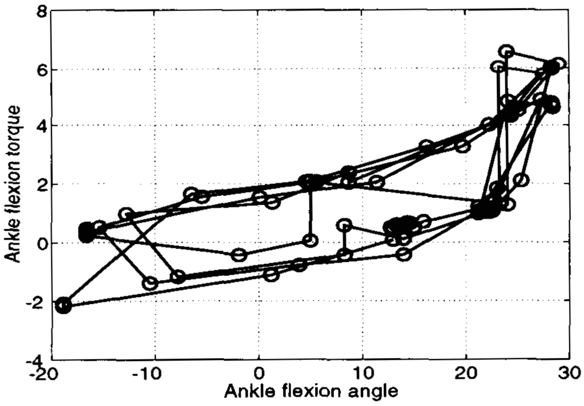

FIGURE 18. Ankle flexion torque vs. angle, 4 repetitions.

Database coverage

The space suit database compiled in this work covers a larger range of joint angles than any other previous study on space suit joint torques. Angle ranges for which angle and torque data was obtained are shown in

Figure 19. The gray rectangles in Figure indicate the range of motion that was specified for the design of the EMU, or the robot's range of motion for the humerus rotation, ankle rotation and ankle inversion joints, where the EMU range of motion was unspecified. The robot's range of motion coincides with the EMU design specification in most joints, except the shoulder abduction joint. The robot's shoulder abduction joint has a range of 0 deg-90 deg, which is less than the EMU design specification. The robot can, however, position its arm above its shoulder level by using the shoulder flexion joint, but it cannot measure true shoulder abduction joint torques in this configuration. Another instance in which the space suit design range of motion is much greater that the database range is the humerus rotation joint. The human test subjects did not exceed 50 deg of positive humerus rotation angle, even though the robot can accomplish a positive humerus rotation of 90 deg. Published data on the range of motion of unsuited individuals for humerus rotation motions indicates that the 50th percentile humerus rotation limit in the positive direction is approximately 60 deg, and the 95th percentile positive limit is 97 deg.[2] It is likely, then, that a 90 degree humerus rotation would not have been achievable by the test subjects, even if they had not been wearing the space suit.

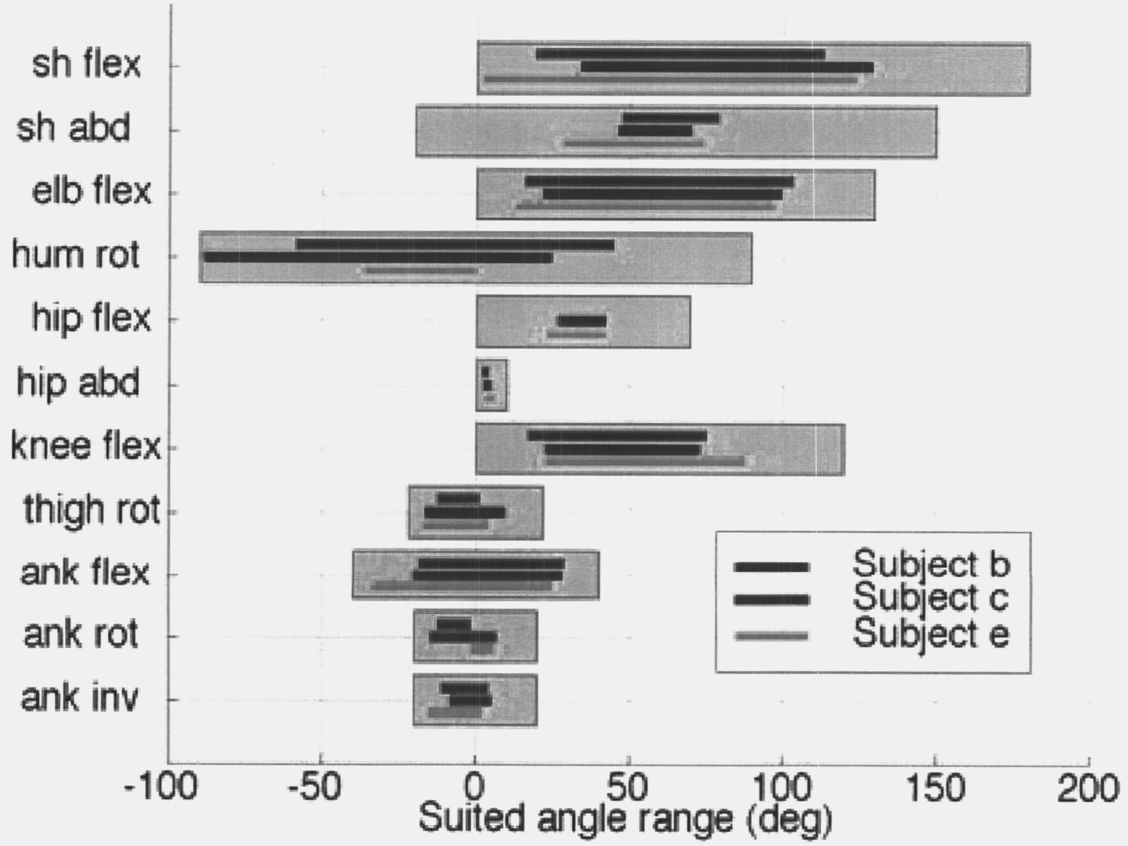

FIGURE 19. Angle range of space suit database compared to space suit design specification for joint range of motion.

A total of 80 motion capture data sets were obtained from the space-suited test subjects, 247 torque data sets were obtained from the suited robot and 337 data sets obtained from the unsuited robot, resulting in over 580 robot torque data sets.

Error analysis

Errors in the torque and angle values come from three sources:

- Motion capture system errors in estimating the human subjects's joint angles
- Robot joint position errors due to imperfect tracking of the trajectory
- Robot torque measurement errors.

Motion capture errors

Estimating the accuracy of off-the-shelf motion capture systems, such as the one used in this study, is difficult. Manufacturers make optimistic accuracy claims and sufficient computational detail is usually not available to the end user to make a detailed error analysis. This analysis is an effort to make a reasonable, but somewhat conservative, estimate of the motion capture system's accuracy in the configuration used in this study.

The motion capture system measures the positions of reflective markers attached to the human test subjects' arm, leg, and torso. Using the Cartesian positions of the markers, the angles between arm and leg segments are calculated. Random errors in measuring marker positions can be propagated through the angle calculations to produce estimates of the angle errors that result from position measurement errors.

The angle calculation is shown in Figure 20. The motion capture system outputs the *x, y, z* position of four points, A, B, C, and D, on two successive arm or leg segments. Using the positions of the four points, vectors r_1 and r_2, along the two body segments, are calculated. The angle between these two body segment vectors, θ, is the joint angle.

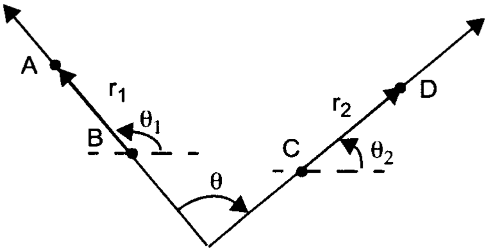

FIGURE 20. Joint angle calculation used for motion capture data.

As shown in Figure 21, the vectors r_1 and r_2 are at angles θ_1 and θ_2 with respect to an arbitrary coordinate reference. The joint angle θ is the difference between θ_1 and θ_2. Focusing on a single body segment vector illustrates how errors in measuring the positions of points A-D relate to angle errors. Figure shows body segment vector r_1, with point A' displaced from point A by an error *d*, perpendicular to r_1.

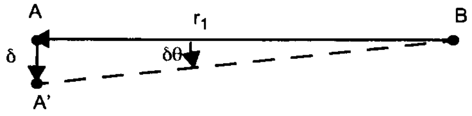

FIGURE 21. Joint segment vector with measurement error δ.

The difference in angle between segment BA and segment BA' is given by

$$\delta\theta \approx \sin(\delta\theta) = \frac{|\underline{\delta}|}{|\underline{r_1} + \underline{\delta}|} = \sqrt{\frac{\delta^2}{r_1^2 + \delta^2}} \qquad \text{Eq 7}$$

If d_2 is the variance of the error in measuring r_1, then

$$var(\delta\theta_1) = \frac{\delta^2}{r_1^2 + \delta^2}. \qquad \text{Eq 8}$$

By the same reasoning, the variance of the error in θ_2 is

$$var(\delta\theta_2) = \frac{\delta^2}{r_2^2 + \delta^2}. \qquad \text{Eq 9}$$

Therefore, the variance of the error in measuring θ is given by

$$var(\delta\theta) = var(\delta\theta_1) + var(\delta\theta_2) = \frac{\delta^2}{r_1^2 + \delta^2} + \frac{\delta^2}{r_2^2 + \delta^2} \qquad \text{Eq 10}$$

Equation 10 shows that errors in joint angle estimation increase when marker position estimation errors increase and decrease when the markers on a body segment are separated by a greater distance.

The manufacturer of the motion capture system claims that marker positions are determined with errors on the order of millimeters. The high accuracy claim may apply to the most favorable configurations, but the motion capture data acquired in this study is not likely to be that accurate. The markers used in this study were hemispheres of diameter 1 cm. It is reasonable to assume that, under good visibility conditions, the markers are accurately located to within one diameter, or 1 cm.

Because the markers were blocked from the camera's view at times, redundant markers were used. Each of the points A, B, C, and D in Figure is a position calculated by taking the means of the positions of two markers that were placed on a band around a test subject's arm or leg. Averaging marker positions improves accuracy, but, since markers were sometimes obscured, the full eight-marker accuracy was not obtained at all times. When two markers are available to be averaged, the variance of the error in calculating the position of point A, B, C or D is 0.5 cm^2, while when only one marker is available, the position error variance is 1 cm^2. Table shows the angle error standard deviation for r_1 and r_2 dimensions typical of several joints, for different numbers of visible markers. It is assumed that r_1 and r_2 span 0.75 of the length of the arm or leg segment. At least four markers must be visible in order to calculate an angle between the two segments.

TABLE 8. Angle error estimates for different numbers of visible markers

	Joint angle error standard deviation (deg)				
Joint	8 markers	7 markers	6 markers	5 markers	4 markers
Elbow	3.7	4.2	4.6	5.0	5.3
Knee	2.8	3.3	3.5	3.8	4.0

Robot trajectory tracking errors

The motion capture data from the human subjects was used as trajectories for the robot to follow in both suited and unsuited torque data collection. Errors in trajectory following were caused by loads imposed by the space suit and timing issues with the RSSTA software application.

The space suit imposed significant loads on the robot as it attempted to follow the trajectories. As a result, the amplitudes of some of the motions were reduced on the robot, particularly in the shoulder abduction and hip flexion joints, where the loads due to the robot and space suit's weight and the space suit's stiffness were largest. The lack of stiffness of the robot's joints effectively limited the range over which the joint could be positioned when the space suit was on the robot. Because the RSSTA application does not allow the user to command joint deflections that are outside the robot's limits, the actual joint angle that was obtained when the maximum joint angle was commanded was the effective limit. This problem can be remedied in the future by tuning the servo gains on the robot's shoulder and hip joints to have higher position error gains. Effects of tracking errors when the robot was wearing the space suit are shown in Figure 22, where the percentage of unsuited joint angle range that was achieved in suited data collection is plotted for each of the 11 simple motions.

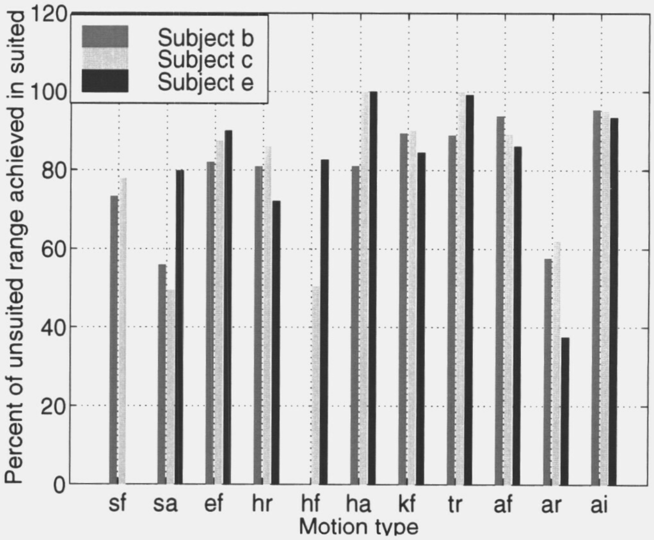

FIGURE 22. Percentage of unsuited range achieved in suited robot trials.

An additional source of error in robot trajectory following arose from timing issues. When the robot was programmed to follow motion capture data trajectories at full speed, the joint angle data recorded by the robot indicated in many cases that the robot actually moved slower than the command trajectory. The duration of the data file exceeded the duration of the trajectory file and it appeared that samples were being dropped while the robot was performing motions. The robot would hold all joints in the same positions for 2-3 samples at a time, then proceed with the motion. The number of "held" samples corresponded to the excess time taken in executing the motions. Less sample dropping occurred when trajectories were run at lower speeds. To produce better matching of the robot's motions to the command trajectories, suited and unsuited data was collected for all trajectories at both full speed and half speed.

The angle data in the space suit torque-angle database is the robot's actual position, not the commanded position, so tracking errors have the effect of slightly distorting the motions that the robot performed; tracking errors do not cause errors in the measured angles in the space suit database. Figure 23 shows root mean square (RMS) differences between suited and unsuited robot joint angles, plotted by trial type. The RMS errors, which range from 0.5 deg to 3 deg, are of the same order of magnitude as the motion capture data errors listed in Table 8.

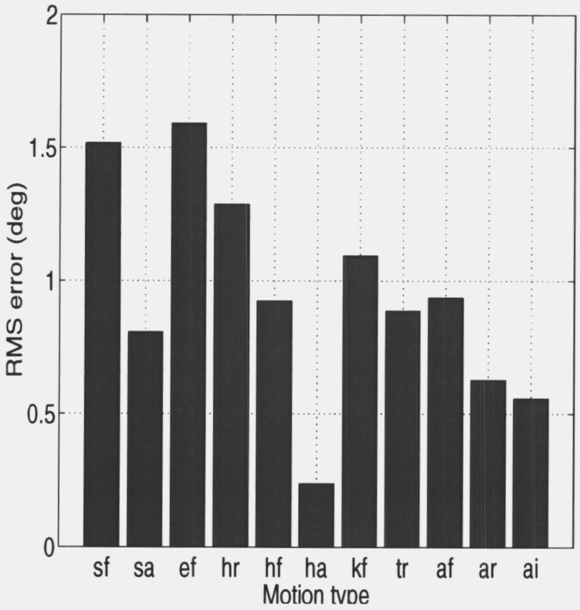

FIGURE 23. Mean RMS angle differences between suited and unsuited robot motions.

Torque measurement errors

Errors in torque measurement arise from bias, noise, and quantization. The robot's load cells were calibrated when it was originally set up at Johnson Space Center. These calibration factors were in use when suited and unsuited data was collected with the robot. The load cell calibrations were again evaluated after the data collection by applying known torques to each load cell and comparing the RSSTA torque output to the known applied torque. The later assessment indicated that calibration factor errors were all less than 4%.[13]

Noise and quantization effects interact to result in a random error of approximately 0.113 Nm (1 inch pound) in all joints. Torque values are represented in the RSSTA software as integers in the units of inch pounds, reducing the resolution by as much as a factor of 10, compared to the hardware-imposed resolution limits, in some cases. As a result, the resolution of the torque data depends on the calibration factor for each joint. The resolution is the larger of the torque corresponding to 1 A/D count or 1 inch pound (0.113 Nm). For all joints except the hip flexion joint, the torque resolution is 0.113 Nm; the torque resolution for the hip flexion joint is 0.226 Nm.

3.7 Database contributions

The objective of the experimental portion of this research effort was to compile an extensive database of the torques required to bend the joints of a space suit, in realistic, human-generated motions. The experiments were carried out in two phases, with both human test subjects and an instrumented robot. Human test subjects wearing the space suit performed 20 simple and complex motions, while joint angles of their arm and leg were recorded using video motion capture. The space suit was then installed on an instrumented robot, which was driven to reproduce the human subjects motions while joint torques were recorded. Because the robot had never been used with a space suit, several modifications were made to the robot to allow the space suit to fit on the robot and protect both from damage. Contributions due to the weight of the space suit and robot were subtracted from the torque data, resulting in a consistent set of space suit joint torques and joint angles in realistic motions, with angles accurate to approximately 2 deg-5 deg and torques accurate to approximately 0.1 Nm.

The database compiled in this work is more extensive than any other published space suit torque-angle database, covering 11 joints over a large range of angles. Realistic, three-dimensional human-generated motions were used for data collection. Because torque data was collected by the robot as a surrogate for a human occupant of the space suit, the torques measured in this study are more representative of realistic conditions than data from previous studies that measured joint stiffnesses for empty, pressurized space suits. The space suit torque-angle database serves as a basis for developing and validating both mathematical and physical models of space suit joint mobility characteristics.

4.0 Modeling

The space suit torque-angle database described in Section 3.0 presents a unique opportunity to develop models of space suit mobility and verify them against experimental data. Models of space suit mobility are useful in two applications: numerically predicting the torque required to bend a space suit's joints and understanding the physical processes that determine how mobile a space suit's joints are. These two applications require two different modeling approaches: first, a descriptive mathematical modeling technique based on experimental data and second, a theoretical model based on physical principles. Section 4.0 describes two modeling efforts: a mathematical model based on empirical data that predicts the torque required to bend the space suit's joints and a comparison between two physics-based models of bending pressurized cylinders and the space suit torque angle database compiled in Section 3.0. The opportunity to validate the mathematical and physical models against experimental data is a unique aspect of this research effort.

4.1 Mathematical modeling

The Preisach model The Preisach hysteresis model reproduces a hysteresis curve by summing contributions from the simplest possible hysteresis transducers. The primitive hysteresis transducer, $\hat{\gamma}(\alpha, \beta)$, has an output value equal to either +1 or -1. For increasing inputs, the output switches from -1 to +1 at an input value of α, and for decreasing inputs, the output switches from +1 to -1 at an output value of β.

To construct more complicated hysteresis transducers with continuous, non-unity outputs, the Preisach model uses a weighted sum of simple hysteresis operators. The weighting function $\mu(\alpha,\beta)$ is defined as a function of the combination of upward and downward switching values, α, β, of the hysteresis transducer. The Preisach function, $\mu(\alpha,\beta)$, is defined for all $\alpha > \beta$, $-\alpha_0 < \alpha < \alpha_0$, and $-\alpha_0 < \beta < \alpha_0$, forming a triangle in α–β space.

Construction of the output of the composite hysteresis transducer is done by integrating the individual $\hat{\gamma}_{\alpha,\beta}$ values, as shown in Equation 11.

$$f(t) = \iint_{(\alpha > \beta)} \mu(\alpha, \beta)\hat{\gamma}_{\alpha, \beta}u(t)d\alpha d\beta \qquad \text{Eq 11}$$

Calculation of $f(t)$ is aided by a graphical representation of the α-β space. The weighting function $\mu(\alpha,\beta)$ is defined over the triangle that is bounded by the $\alpha=\beta$ line and the maximum values of α and β, α_0 and β_0, which are defined by the saturation limits of the output. To obtain $f(t)$, Equation 11 is integrated over this triangle.

To perform the integration in Equation 11,the triangle may be subdivided into two sets:

- Region S+, where corresponding $\hat{\gamma}_{\alpha,\beta}$ operators are "up", or equal to +1
- Region S-, where corresponding $\hat{\gamma}_{\alpha,\beta}$ operators are "down", or equal to -1

Substituting +1 for $\hat{\gamma}_{\alpha,\beta}$ in the S^+ region and -1 for $\hat{\gamma}_{\alpha,\beta}$ in the S^- region, Equation 11 simplifies to

$$f(t) = \iint_{S^+}\mu(\alpha, \beta)d\alpha d\beta - \iint_{S^-}\mu(\alpha, \beta)d\alpha d\beta . \qquad \text{Eq 12}$$

Equation 12 can be integrated if the boundary between the S^+ and S^- regions is known. The input history is stored by drawing the boundary between the S^+ and S^- regions. The boundary is drawn by constructing line segments in a staircase pattern within the triangle based on the value of the input $u(t)$ and whether the input is increasing or decreasing. The boundary is drawn according to the following rules:

1. The boundary starts on the $\alpha=\alpha_0$ segment if the initial input is descending and the $\beta=-\alpha_0$ segment if the initial input is ascending.
2. Subsequent boundary segments are drawn horizontally or vertically depending on whether $u(t)$ is increasing or decreasing:
    - Increasing $u(t)$: horizontal line segment at $\alpha=u$
    - Decreasing $u(t)$: vertical line segment at $\beta=u$
3. A boundary segment is obsolete if its α value is less than the α value of a later segment having the same β value or if its β value is less than the β value of a later segment that has the same α value.
4. The last line segment ends on the $\alpha=\beta$ line.

An exploration of the Preisach hysteresis model focused on four of the important features of the outer hysteresis curve shape: number of loops, direction of loops, separation between increasing and decreasing curves and dT/du, resulting in several important insights. The proper choice of $\mu(\alpha,\beta)$ can produce single or multiple hysteresis loops, in either clockwise or counterclockwise directions. The separation between increasing and decreasing curves can be written as an integral of $\mu(\alpha,\beta)$ over a region in the top left corner of the α–β space. Thus, high amplitudes of $\mu(\alpha,\beta)$ in the top left corner of the α–β space, where α is near α_0 and β is near $-\alpha_0$, result in large separations between the increasing and decreasing output curves.

Model identification The model identification process for the Preisach model involves calculating the weighting function $\mu(\alpha,\beta)$ from experimental data. The central premise of the Preisach model identification methods is that the difference between two output values is equal to the integral of $\mu(\alpha,\beta)$ over a region whose bounds are known from the input history. Calculating the integrated $\mu(\alpha,\beta)$ for a sufficient number of regions allows the Preisach model to be implemented to predict the hysteretic system's output as a function of its input and input history. The following derivation shows how the integral of $\mu(\alpha,\beta)$ over a region with known bounds can be calculated from the difference between two output values.

The input to the hysteresis transducer begins below the low input limit, $-\alpha_0$, and increases to a value u_1, which is below the high input limit. The corresponding output, when $u=u_1$, is $T=T_1$. In the α-β plane, the S^+/S^- boundary lies at $\alpha=u_1$. The input then decreases from $u=u_1$ to $u=u_2$, and a vertical segment is added to the S^+/S^- boundary at $\beta=u_2$. The output when $u=u_2$ is $T=T_2$.

According to 12, the output $T(u)$ is equal to the integral of $\mu(\alpha,\beta)$ over the S^+ region minus the integral of $\mu(\alpha,\beta)$ over the S^- region. Using 12 to calculate the difference between T_1 and T_2 results in the following expression for the output difference, in terms of the S^+ and S^- regions at $u=u_1$ and $u=u_2$.

$$
\begin{aligned}
T_1 - T_2 &= T_{max} - 2 \int\int_{S^-_1} \mu(\alpha, \beta) d\alpha d\beta \\
&\quad - \left[T_{max} - 2 \int\int_{S^-_2} \mu(\alpha, \beta) d\alpha d\beta \right] \\
T_1 - T_2 &= 2 \int \int_{S^-_2 - S^-_1} \mu(\alpha, \beta) d\alpha d\beta
\end{aligned}
\qquad \text{Eq 13}
$$

The difference between integration areas, S^-_2-S^-_1, for $u=u_2$ and $u=u_1$, is a triangle that has vertices at (u_1,u_2), (u_1, u_1) and (u_2, u_2). When the input decreases from u_1 to u_2, the difference in output values is equal to the integral of $\mu(\alpha,\beta)$ over the triangle.

Numerical Implementation To determine $\mu(\alpha,\beta)$ from output differences, Mayergoyz[26] suggests differentiating the output data twice with respect to the input. Taking two derivatives of measured data values would amplify random noise to unacceptable levels, so the method that Mayergoyz[26] recommends is not practical.

An alternative Preisach model identification scheme, developed by Doong and Mayergoyz[8] and further explained by Ge and Jouaneh[11], is based on the same premise, but avoids differentiating data in the identification step and double integrations in the implementation step. This method avoids differentiation and integration by calculating the integral of $\mu(\alpha,\beta)$ over a collection of triangles in α–β space from output differences, then uses sums and differences of the triangle integrals to construct the output for any input history.

According to Equation 13, the integral of $\mu(\alpha,\beta)$ over a triangle bounded by the $\alpha=\beta$ line and the $\alpha=u_1$, $\beta=u_2$ point is equal to T_1-T_2, as long as the input increased from its lower limit to u_1, then reversed direction and decreased to u_2, with no other direction reversals. This relationship allows the integral of $\mu(\alpha,\beta)$ to be calculated based on the appropriate output differences for triangles bounded by the $\alpha=\beta$ line and any point inside the large triangle over which $\mu(\alpha,\beta)$ is defined. The quantity $X(\alpha_1,\beta_1)$ is defined as the integral of $\mu(\alpha,\beta)$ over a triangle bounded by α_1, β_1 and the $\alpha=\beta$ line. If u increases from its low limit, reverses direction at $u=\alpha_1$, then decreases to β_1, $X(\alpha_1,\beta_1)$ is given by

$$
\begin{aligned}
X(\alpha_1, \beta_1) &= (T(u = \alpha_1) - T(u = \beta_1)) \\
X(\alpha_1, \beta_1) &= 2 \int_{\beta_1}^{\alpha_1} \int_{\beta}^{\alpha_1} \mu(\alpha, \beta) d\alpha d\beta
\end{aligned}
\qquad \text{Eq 14}
$$

If $X(\alpha,\beta)$ is known for all $-\alpha_0<\alpha<\alpha_0$, $-\alpha_0<\beta<\alpha_0$, $\alpha>\beta$, then $X(\alpha,\beta)$ values can be added and subtracted to construct any Preisach model output, provided that the boundary between S^+ and S^- is drawn according to the rules described above. The integral of $\mu(\alpha,\beta)$ over S^+ is given by:

$$
T = -X(\alpha_0, -\alpha_0) + \sum_{i=1}^{n} -1^{n+1} X(\alpha_i, \beta_i) \qquad \text{Eq 15}
$$

Error Analysis Because the hysteresis model coefficients are determined from experimental data, random errors in the experimental data lead to random errors in the model output whose statistical properties can be predicted. The error analysis provides a method for generating confidence intervals for the Preisach model output if the model is identified and implemented according to the Doong and Mayergoyz[8] method.

According to Equation 15, the Preisach model output is the sum of positive and negative $X(\alpha,\beta)$ values at the vertices of the S^+/S^- contour. Assuming that the errors in the experimental torque and angle data that was used to calculate $X(\alpha,\beta)$ are random, white noise, errors in

X(α,β) should be uncorrelated with errors in *X* at other values of α and β. Thus, the variance of the model output *T* is equal to the sum of the variances of the individual *X(α,β)* values that were summed to obtain *T*.

Summing the variances of the *X* values at the *n* S^+/S^- boundary vertices results in the variance of the model output *T*. The variance of the measured torque is σ^2_T and the variance of the measured angle is σ^2_A.

$$var(T) = (2n)\sigma_T^2 + \sigma_A^2 \sum_{i=1}^{n} \left(\frac{\partial X_i}{\partial \alpha_i} + \frac{\partial X_i}{\partial \beta_i}\right)^2 \qquad \text{Eq 16}$$

4.2 Results: Hysteresis modeling

Preisach model coefficients *X(α,β)* were fitted to the first-order transition curves that were produced for space suit torque-angle data. Model coefficients were obtained for elbow flexion, hip abduction, hip flexion, knee flexion, ankle rotation, and ankle flexion motions. These experimentally-determined model coefficients were then used to predict the torques required to bend the space suit joints for motions produced by space-suited human subjects, then the torque predictions generated by the model were compared to experimental data.

The Preisach model coefficients are defined in terms of the upward and downward switching thresholds, *α* and *β*, of the primitive hysteresis transducers. The model coefficients, X(*α*,*β*), can be plotted in three dimensions vs. *α* and *β*, over the triangular region for which *α* and *β* are defined: $-\alpha_0<\alpha<\alpha_0$, $-\alpha_0<\beta<\alpha_0$, $\alpha>\beta$. The experimentally-determined model coefficients for the elbow flexion, hip abduction, hip flexion, knee flexion, ankle rotation, and ankle flexion joints are plotted in Figure 24 – Figure 29.

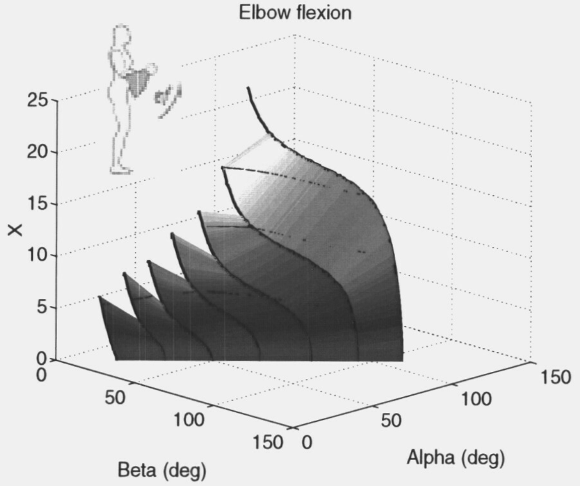

FIGURE 24. Preisach model coefficients plotted vs. α and β for the elbow flexion joint.

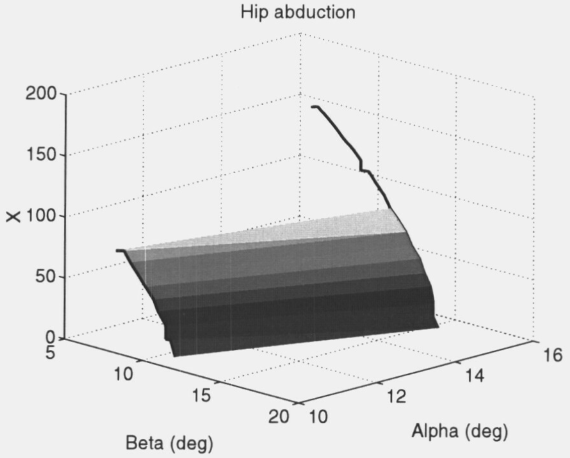

FIGURE 25. Preisach model coefficients plotted vs. α and β for the hip abduction joint.

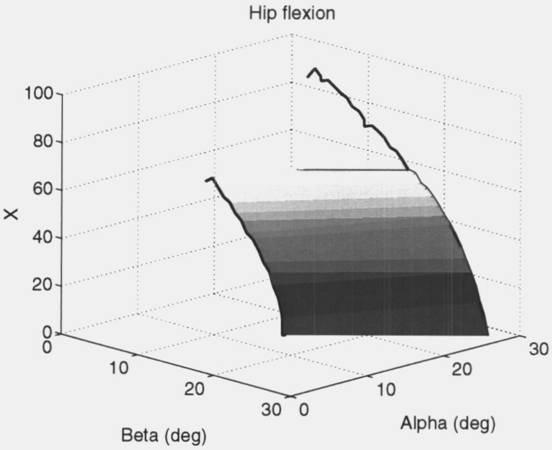

FIGURE 26. Preisach model coefficients plotted vs. α and β for the hip flexion joint.

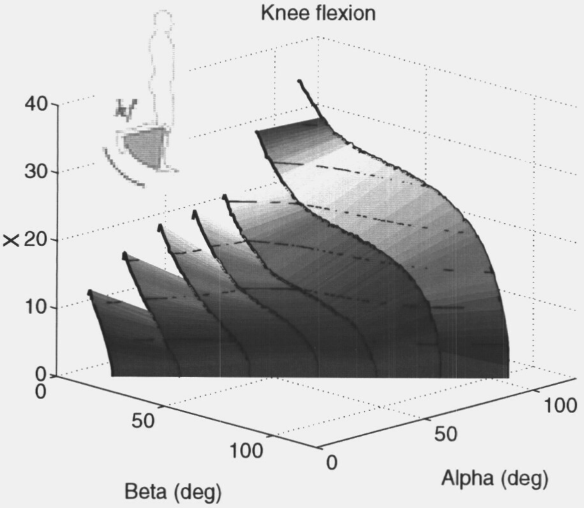

FIGURE 27. Preisach model coefficients plotted vs. α and β for the knee flexion joint.

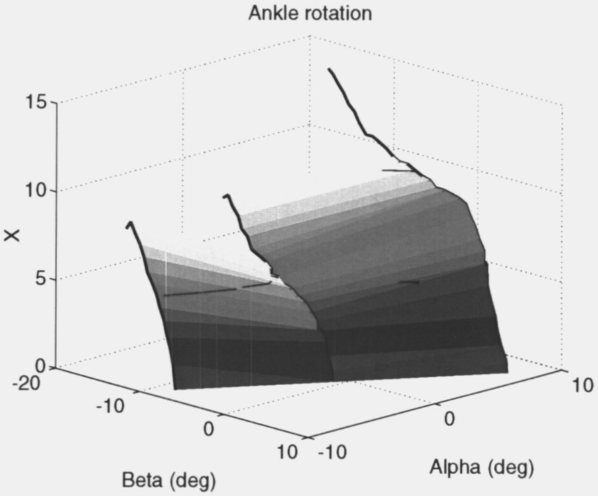

FIGURE 28. Preisach model coefficients plotted vs. α and β for the ankle rotation joint.

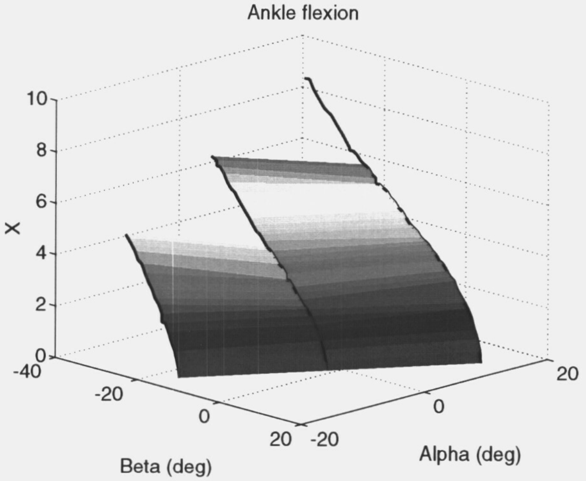

FIGURE 29. Preisach model coefficients plotted vs. α and β for the ankle flexion joint.

The hysteresis models were implemented for each joint and compared to experimental torque-angle data for motions that were generated by space-suited human subjects. Joint angle data from the human subjects was used as an input for the hysteresis model, which generated a torque prediction as well as a 95% confidence interval on the prediction. The experimental joint torque data is compared to the model predictions and confidence intervals for the elbow in Figure 30 and for the knee in Figure 31.

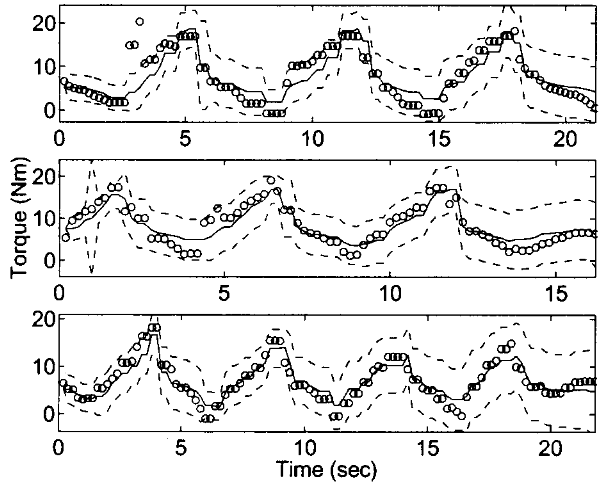

FIGURE 30. Elbow flexion torque compared to hysteresis model prediction for subjects B (top), C (middle), and E (bottom).

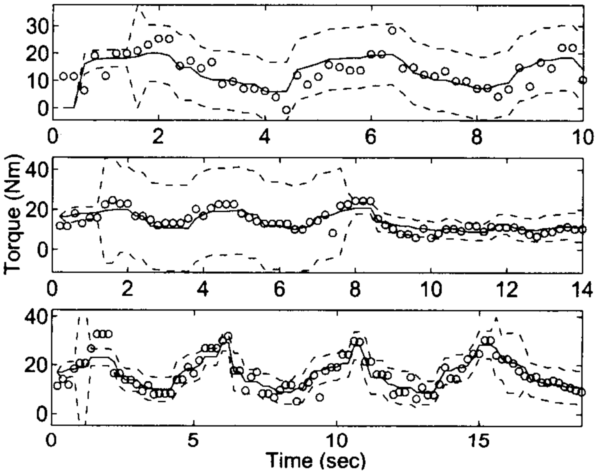

FIGURE 31. Knee flexion torque compared to hysteresis model prediction for subjects B (top), C (middle), and E (bottom).

The Preisach model outputs match well with data for elbow flexion, hip abduction and knee flexion, with $R^2>0.6$ for these joints. The error estimates generated appear to be a reliable, or at least conservative, estimate of the error standard deviations.

The Preisach hysteresis model is a useful tool for predicting the torque needed to bend space suit joints as a function of time for complicated angle trajectories. The ability to reproduce realistic space suit torques dynamically makes the Preisach model well-suited for use in dynamic simulation of EVA tasks. The experimental data reported in Chapter 3 as well as other investigators' data indicate that the torque-angle relationship for space suit joints is markedly hysteretic. Consequently, reproducing dynamic behavior of space suit joints requires a model that captures hysteresis; other modeling techniques such as linear regressions on angle and angular velocity will not accurately predict the effects of the angle history on the torque required to bend the space suit's joints.

The Preisach hysteresis model has some limitations in modeling space suit joints, however. To identify the model coefficients, it is necessary to vary the input between several distinct minima and maxima. Because of this, the model identification process is not well-suited to human-generated motions, although characteristics of human-generated motions, such as range and speed, can be incorporated into the input data for realism. Another limitation of the Preisach model is that the maximum input and output are set when the model coefficients are identified. When the model is implemented later, if the input exceeds the previously-set maximum, the output saturates and errors between the model prediction and actual torques may become large. Modeling the hysteretic characteristics of space suit joints is essential for making accurate predictions of the torques required to bend the space suit joints in dynamic situations. This work demonstrates that the Preisach hysteresis model accurately reproduces torques needed to bend space suit joints.

4.3 Physics-based modeling

Beam model The beam model, which was developed by Comer and Levy[3] and extended by Main, Peterson, and Strauss[22-25], treats a pressurized cylinder as a long, slender member, loaded in a single plane, whose behavior is governed by elasticity and buckling phenomena. The central idea of the beam model is that fabric can sustain only extensional stresses; when the fabric wall of the beam is compressed, it wrinkles and does not contribute to the stiffness of the beam. The beam model predicts the extent of the wrinkled portion of the beam and integrates the extensional stress resultants over the tensioned, unwrinkled, portion of the beam to obtain a moment-curvature relationship for the pressurized beam.[3, 22, 25] Stress resultants are normalized by the thickness of the fabric, and expressed in terms of load per unit length in units of N/m, because fabric stress-strain behavior is not highly correlated with fabric thickness.

The applied loads and the constitutive relations of fabric, which relate stresses and strains and are given in Equation 17, determine the extent of wrinkling in the fabric. In general, fabric is assumed to be orthotropic, with Poisson ratio v and different moduli, E_H and E_L in the hoop and longitudinal directions.

$$\varepsilon_L = \frac{\sigma_L}{E_L} - \frac{\upsilon\sigma_H}{E_L} \qquad \varepsilon_H = \frac{\sigma_H}{E_H} - \frac{\upsilon\sigma_L}{E_L} \qquad \text{Eq 17}$$

The beam model predicts that the fabric wall of the beam wrinkles when the local longitudinal strain, ε_L, becomes negative. Equation 17 shows that the cross-coupling component in the constitutive relations makes the fabric wrinkle at positive values of longitudinal stress, σ_L, when the hoop stress, σ_H, is positive. The hoop loading due to pressurization thus makes the fabric wrinkle at lower applied loads as the beam is bent. The longitudinal stress at which wrinkling occurs is given by:

$$\sigma_L = \upsilon pr \qquad \text{Eq 18}$$

When the fabric is wrinkled, its stress resultant is considered to be zero, because it cannot resist compressive loads. The longitudinal stress is maximum on the outside of the bend and decreases linearly until it reaches the wrinkling limit, then the wrinkling condition sets it equal to zero.

To determine the curvature of the beam, it is first necessary to find the extent of the wrinkled region, using the relation between applied moment, M, internal pressure, p, and beam radius. A polar coordinate frame is defined with $\theta=0$ on the inside of the bend, at the center of the wrinkled region and $\theta=\theta_0$ at the edge of the wrinkled region. The value of θ_0 is given by Equation 19.

$$\frac{M}{pr^3} = \frac{\frac{\pi}{2}[(\pi-\theta_0)+\sin\theta_0\cos\theta_0] +}{\sin\theta_0+(\pi-\theta_0)\cos\theta_0} \qquad \text{Eq 19}$$
$$\frac{-\upsilon[(\pi-\theta_0)^2-(\pi-\theta_0)\sin\theta_0\cos\theta_0-(2\sin\theta_0)^2]}{\sin\theta_0+(\pi-\theta_0)\cos\theta_0}$$

The θ_0 that is calculated by solving Equation 19 numerically for specified M/pr^3 can then be substituted into Equation 20 to obtain the curvature resulting from the applied moment.

$$K = \frac{M-2\upsilon pr^3\sin\theta_0}{Er^3[(\pi-\theta_0)+\sin\theta_0\cos\theta_0]} \qquad \text{Eq 20}$$

In contrast to the beam model, the membrane model treats the fabric cylinder wall as an inextensible material that transmits forces only along its surface and only in tension. Bending deflections of the structure result in changes in its cylinder's cross-sectional shape and the volume that it encloses. The cross-sectional shape of the fabric tube is determined by the assumptions of inextensibility and exclusively tensile loading. These assumptions result in reliable approximations of the tube's shape, even when deflections are large.

Membrane model The membrane model uses a variational principle to relate applied bending moment, force applied at the tube's ends, and the bending angle of the pressurized fabric tube. The potential energy of a tube with volume V, internal pressure p, end force Q, bending moment M, bending angle ϕ and linear displacement δ is given by:

$$\Pi = -pV - Q\delta - M\phi \qquad \text{Eq 21}$$

When the system is at equilibrium, the potential energy is minimized. For the case of pure bending, $Q=0$ and $\delta=0$. The moment-angle relationship that minimizes the potential energy is calculated by holding the bending moment, M, fixed and differentiating the potential energy, Π, with respect to the bending angle ϕ. When $\frac{d\Pi}{d\phi} = 0$, the potential energy is minimized.

$$\frac{d\Pi}{d\phi} = -p\frac{dV}{d\phi} - M = 0$$
$$\Rightarrow M = -p\frac{dV}{d\phi} \qquad \text{Eq 22}$$

Equation 22 shows that the equilibrium bending moment-bending angle relationship is set by the relationship between the internal volume of the tube and the bending angle. The assumptions of inextensibility and tensile loading set the shape of the tube as a function of bending angle. Based on the four principles of membrane shape listed in Reference [10], the shape of the bent tube can be determined. The geometry of a bent pressurized tube is shown in Figure . For a tube of radius R, the radius of the bent outer surface of the tube is $2R$. The inner surface at the bend folds inward, towards the center of the tube, forming a kink in the tube wall. Away from the kinked region, the tube is straight. Points P and S, which lie on the tube wall, are defined to aid in calculating the tube's cross-sectional area. Point P is located on the kink at the inside of the bend, and point S is the corresponding point on the outside of the bend. Point P and point S are the same distance away from the end of the tube. θ is the angle between a line drawn from the inside of the bend to point S and another line that is normal to the straight sides of the tube. The length of the bent portion of the tube on the outer edge is $4R\phi$.

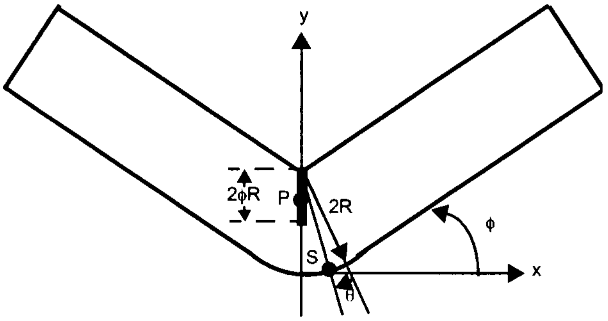

FIGURE 32. Bent tube shape, according to membrane model.

The locations of points P and S are defined as follows.

$$
\begin{aligned}
x_P &= 0 \\
y_P &= 2R(1+\theta) \\
x_S &= 2R(1-\cos(\phi-\theta)) \\
y_S &= 2R\sin(\phi-\theta)
\end{aligned}
\qquad \text{Eq 23}
$$

The distance between points P and S, which can be calculated from Equation 23, and continuity of slope between the rectangular portion and the circular portion of the cross-section allow the cross-sectional area to be calculated as a function of *θ*. The cross-sectional area of the tube is given by Equation 24, as a function of *H*, the distance between points P and S.

$$A(\theta) = \pi\left(R^2 - \left(R - \frac{H(\theta)}{2}\right)^2\right) \qquad \text{Eq 24}$$

The cross-sectional area is integrated over the length of the tube to obtain the bent tube volume. The moment-bending angle relation is obtained by differentiating the volume numerically with respect to *ϕ*, according to 22.

A comparison of the torque-angle predictions of the beam model, membrane model and experimental data from the knee joint is shown in Figure . The membrane model agrees with experimental data within 30 degrees of the knee joint's equilibrium angle, while the beam model's torque predictions do not agree with the experimental data.

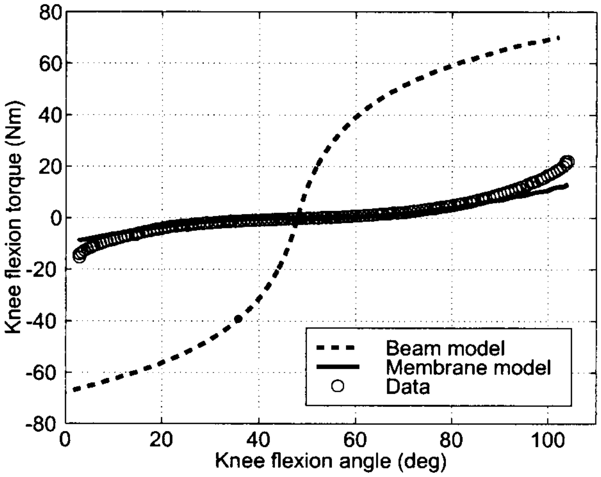

FIGURE 33. Comparison between beam model, membrane model and experimental data for knee joint.

The beam model and membrane model represent opposite extremes of the processes governing space suit joint mobility. The beam model assumes that the space suit joint torque-angle relationship is determined solely by elastic deformations of the fabric wall of the space suit, with no changes in the internal volume of the space suit segment. The membrane model makes the opposite assumptions: that the space suit fabric does not stretch, although the cross-sectional shape deforms, resulting in reduction in internal volume as the joint is bent. According to the beam model, bending moments only stretch the space suit fabric; according to the membrane model, bending moments only compress the gas inside the space suit.

It is reasonable to expect that the actual behavior of a space suit falls between these two extremes, that both elasticity and volume changes determine space suit joint mobility. Comparing these two approximate models to experimental data illustrates where on the continuum between elasticity and volume change the space suit joint behavior falls and indicates whether the space suit behavior can be approximated by one model or the other.

The beam model is inconsistent with experimental data for the elbow and knee joints, both in the bending moment magnitudes predicted and the trend in bending moment with increasing deflection. The beam model predicts bending moments for the elbow and knee joints that exceed the experimental data by at least a factor of 5. In addition, the beam model predicts a decreasing slope of the moment-angle curve as bending angle increases, while the data shows a increasing slope with increasing bending angle.

The shape of the torque-angle curves generated by the membrane model is consistent with the experimental data, because the model's torque-angle curves are flat near the equilibrium position of the joint and increase in slope as deflection increases. The membrane model follows the experimental data over a bending angle range approximately 30-50 degrees from the equilibrium angle, for the elbow and knee joints. Outside of this range, the amplitude of the experimental torque data is greater than the membrane model's predictions. Although the membrane model can predict the torque needed to bend the joints over about half of the available range of motion, the model's underprediction of torques near the extremes of the angle range prevent it from being used to predict a joint's angular range of motion. Other physical processes, including fabric bunching, sideways compression of the space suit arm or leg, and friction between fabric layers, which were not included in the membrane model, likely play an important role in determining the torque needed to bend the space suit joints at high bending angles.

The results of this analysis indicate that elastic deformations of the space suit fabric do not contribute significantly to the torque needed to bend the elbow and knee joints near the equilibrium angle, and the mobility of the EMU elbow and knee joints near their equilibrium angles is not sensitive to changes in the material properties of the fabric. The membrane model predicts that only internal pressurization and joint geometry determine mobility.

5.0 The Work Envelope: Applying space suit modeling to EVA operations

An important issue in planning extravehicular activity (EVA) tasks and evaluating EVA worksites is determining whether astronauts can reach and comfortably work at the desired worksite. A computational work envelope analysis was developed, which utilizes experimental joint angle and torque data measured during space suit experiments and inverse kinematics analysis, to determine the volume in which a space-suited astronaut can comfortably work with one hand. For a point to be within the workspace, it must be visible and not require excessive torques at the shoulder or elbow joints. These constraints were applied by calculating the joint angles required to place the hand on a designated target, determining the torques at the shoulder and elbow that were needed to hold the hand position, then applying joint torque and visibility limits. Work envelopes were generated from both male and female anthropometric data. A sensitivity analysis on joint range of motion and visibility limits showed that increasing the range of the shoulder abduction/adduction joint to allow the arm to move closer to the body centerline greatly increases the work envelope volume. Increasing visibility in the upward and downward directions leads to sizable increases in work envelope volume, while visibility increases in the left and right directions do not increase the work envelope size.

A critical issue that is addressed in planning for extravehicular activities (EVA's) and evaluating EVA worksites is whether the EVA crew can reach and comfortably work at the designated worksite. Reach considerations are important because, in microgravity, astronauts must restrain their bodies in order to exert forces or moments on other objects. In the United States space program, body restraint during EVA is usually accomplished by foot restraints, particularly when tasks require applying significant forces. The articulated portable foot restraint (APFR) used on the international space station (ISS) can be adjusted to accommodate many orientations but can only be attached to the ISS's structure at discrete locations. Because of the constraints on foot restraint placement, it is essential to determine in the planning process whether a work site is reachable from an available foot restraint location. Although foot restraints are not the only available method of providing body restraint, the necessity of restraining the body for microgravity work makes the problem of providing both adequate restraint and access to the worksite a universal one in microgravity, both inside and outside the spacecraft. A work envelope analysis that incorporates the mechanics of the space suit is a useful method for both assessing potential worksite locations and evaluating the functional significance of modifications to space suit mobility and visibility.

A reach envelope is the region in three-dimensional space that a person can reach. The work envelope is a subset of the reach envelope, representing the volume in which a person can comfortably work. Reach and work envelopes depend on the size and flexibility of the individual. A standard practice is to size workspaces to accommodate the reach and work envelopes of individuals at the extremes of the expected size range, for example, 5th percentile females and 95th percentile males.[29] Most work envelopes are determined experimentally, by measuring how far people of different sizes can reach and obtaining subjective information about the difficulty of working with the hands in different locations. The results of empirical work envelope studies are typically a set of boundaries within which a specified percentage of the intended population can work comfortably. An alternative approach to reach envelope analysis has been developed recently, which uses robot kinematic analysis methods to determine the boundaries within which a person can reach with prescribed limits on joint ranges of motion.[15, 17, 36] Reach envelopes that are determined computationally can be tailored to specific individuals or populations of people.

This report describes a novel work envelope analysis method, which combines inverse kinematics and a model of space suit mobility, enabling the work envelope of a space-suited astronaut to be assessed in greater detail and with more generality than experimental methods allow. The computational work envelope analysis extends the inverse kinematics reach envelope work by prior investigators[15, 17, 36] to determine feasible working positions, which is a more restrictive category than reachable positions, incorporating human strength limits and visibility considerations. The model of space suit mobility developed in this work, which is derived from experimental data, predicts the torques needed to maintain static positions of the space suit arm joints.[33,34]

The work envelope analysis is based on previously described space suit joint mobility experimental data as well as incorporates the torque model. Torques required to maintain the space suit shoulder flexion, shoulder abduction, and elbow flexion joints were calculated using a linear regression model, which predicts torque as a function of joint angle and angular velocity, as shown in Equation 25.

$$\text{Torque} = k_1 + k_2 \times \text{angle} + k_3 \times \text{angular velocity} \qquad \text{Eq 25}$$

Values of k_1, k_2, and k_3 and the regression statistics R^2 and standard error of the fitted torque are given in Table 9[33].

Table 9: Torque model coefficients[33]

Joint	k_1 (Nm)	k_2 (Nm/deg)	k_3 (Nm/(deg/sec))	R^2	standard error (Nm)
Shoulder flexion	-23.4	0.222	0.120	0.777	4.39
Shoulder abduction >50 deg	-75.5	1.20	0.372	0.743	6.42
Shoulder abduction <50 deg	-27.2	0.303	0.110	0.899	0.553
Elbow flexion	-9.04	0.155	0.0380	0.823	2.12

5.1 Work envelope criteria

Three criteria determine whether a proposed hand position is in the work envelope: the torques that are needed to hold the required arm configuration, visibility, and the shape of the resulting work envelope boundaries. The shape of the work envelope is considered because highly convoluted work envelope boundaries are difficult to use, since they are excessively sensitive to the relative positions of the EVA astronaut and the worksite. However, adding the shape criterion overconstrains the problem; as a result, a single torque limit cannot be enforced uniformly. To address this issue, a smoothing algorithm is incorporated to systematically trade off the joint torque and work envelope shape criteria.

Joint torque limits

In order for a person to work for several minutes in a particular arm configuration, the torques needed at all of the arm joints should be low enough that fatigue does not prevent the person from maintaining the desired arm position. The strength measure of interest in a work envelope analysis is the maximum torque that can be sustained for several minutes in a static position. In a survey of research on muscle fatigue, Astrand reported that the maximum force in static, isometric (constant position) muscle contractions can be held for only a short period of time, but 15% of the maximum force can be held for at least 10 minutes, 30% of the maximum torque can be held for approximately 3 minutes, and 50% of the maximum force can be held for 1.5 minutes.[3]

Isometric strength data for shoulder flexion, shoulder abduction, humerus rotation, and elbow flexion motions in both positive and negative directions, which are defined in Figure 3, are shown in Table 10[5]. Torque limits used in the work envelope analysis are based on the limits in Table 10.

TABLE 10. Isometric strength limits for shoulder and elbow.[5]

Motion	50th percentile male (Nm)	95th percentile male (Nm)	50th percentile female (Nm)	95th percentile female (Nm)
Shoulder flexion (+)	71	101	37	57
Shoulder flexion (-)	67	115	30	54
Shoulder abduction (+)	67	103	33	57
Shoulder abduction (-)	92	119	40	60
Elbow flexion (+)	77	111	41	55
Elbow flexion (-)	46	67	27	39

"Low torque" and "excessive torque" limits are set for each joint and direction based on the relationship between maximum holding time and percentage of maximum isometric torque. An arm position for which no joint torque exceeds 15% of the maximum torque is considered "low torque". An arm position which requires more than 30% of the maximum torque from any joint is considered "excessive torque".

Visibility

The space suit helmet and the display and control module (DCM), which is located on the front of the space suit, limit a space-suited astronaut's field of view. A suited astronaut's field of view is limited in the upward and left-right directions by the space suit helmet and visor and in the downward direction by the DCM and the mini-workstation, which is a tool rack located on the front of the hard upper torso (HUT). Only points that are within the field of view are included within the work envelope.

Field of view limits for the EMU space suit published in a NASA EVA interface requirements document entitled NSTS-07700[1] were used in the work envelope analysis. Although the mini-workstation obstructs downward visibility, the NSTS-07700 visibility limits do not include the presence of the mini-workstation. Consequently, the analysis presented herein does not consider the downward visibility limitations imposed by the mini-workstation.

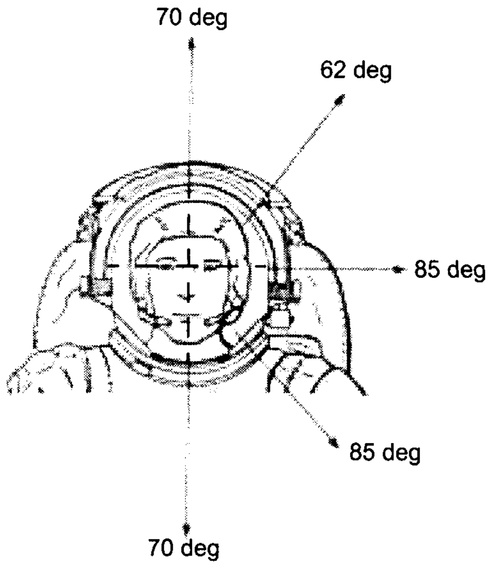

FIGURE 34. Extravehicular Mobility Unit field of view[1]

Work envelope shape

Using an arbitrary torque limit level to determine whether points are inside the workspace results in a work envelope with a complex and convoluted shape. A work envelope with such a complicated shape is difficult to implement in planning EVAs or designing EVA workstations. Small changes in the relative positions of the EVA astronaut and worksite may shift the worksite into or out of the work envelope. Excessive sensitivity to positioning is unwarranted because the appropriate maximum torque levels depend on the strength and fatigue level of the astronaut, the duration of the task, and the accuracy of arm motions required in the task. Furthermore, a complicated work envelope boundary requires storing a large number of boundary vertices for computational implementation, and is difficult to visualize. Therefore, the boundaries of the work envelope should be as simple as possible, while including the maximum number of low-torque points and excluding all excessive-torque points.

The shape of the work envelope is set by categorizing possible points, based on visibility and required torques, as "always include", "always exclude", and "possibly include". Points that are visible and require torques that do not exceed a specified low torque limit are in the "always include" category, points that are not visible or require any joint torque to exceed a specified excessive torque limit are in the "always exclude" category, and points that are visible and require torques that fall between the low torque and excessive torque limits are in the "possibly include" category. The initial boundary is drawn to include only the "always include" points. Then the boundary is smoothed by adding a limited number of points that are in the "possibly include" category. Work envelope boundary smoothness is assessed by determining how many vertices are needed to draw a piecewise-linear boundary around the work envelope region using the contourc algorithm in Matlab (The Mathworks, Natick, MA). Minimizing the number of vertices needed to draw the boundary results in the smoothest boundary.

Arm model

The arm model chosen for the inverse kinematics calculations is a simplified approximation of the complex mechanics of the human arm. The number and type of articulations of the model arm were chosen to coincide with the joints included in the space suit model and to limit the kinematic redundancy of the model arm. The model arm includes four joints: shoulder flexion (sf), shoulder abduction (sa), humerus rotation (hr), and elbow flexion (ef).

The lengths of the arm segments are set based on anthropometric data[29], which is listed in Table 11. The lower arm segment length is the elbow to wrist distance plus half the hand length. Arm segment lengths can also be customized to a specific person.

TABLE 11. Arm segment lengths[29]

Segment	Male, 50th percentile (cm)	Male, 95th percentile (cm)	Female, 50th percentile (cm)	Female, 95th percentile (cm)
Upper arm	36.6	39.4	29.8	32.4
Lower arm	38.3	41.6	33.1	35.3

5.2 Work envelope methods

The visibility and joint torque limitations are applied in a five-step process. First, visibility is evaluated: if the target point is outside of the field of view, it is excluded from the work envelope. Second, inverse kinematics is used to determine the joint angles at the shoulder and elbow that are needed to place the hand on target. The inverse kinematics solution is not unique, because three coordinates of hand position determine four joint angles. The inverse kinematics analysis outputs a set of several arm configurations that put the hand on target. Third, the space suit torque-angle model accepts these joint angles as inputs and calculates the joint torques required to maintain the specified arm configuration. Fourth, the joint torques are compared to the pre-set torque limits and the arm configurations for which no joint torques violate the torque limits are returned as feasible arm positions. If at least one feasible arm position exists for a target hand position, the target point is considered to be within the work envelope. Finally, the overall difficulty of reaching the target point is assessed by calculating a reach difficulty metric, based on the required joint torques. The feasible arm configuration that has the lowest reach difficulty metric is recorded for each target position in the work envelope.

Visibility

Visibility of the target point is evaluated first, because the visibility constraint eliminates a large portion of the possible target points. Visibility is evaluated by locating the suited person's eyepoint relative to the right shoulder, then using the eyepoint position and target hand position to determine whether the target hand position lies within the angular field of view limits defined in Figure 34. A single point that represents the eyepoint position is located on the body centerline, halfway between the eyes. The eyepoint coordinates that were used for 50th and 95th percentile males and females are listed in Table 12.[29] No anthropometric data was available for the position of the eyes forward of the shoulder, therefore, a distance of 10 cm was used in all cases.

TABLE 12. Eyepoint position relative to the right shoulder[29]

Percentile	M 50th	M 95th	F 50th	F 95th
Vertical (cm)	16.5	16.9	15.9	16.5
Left-right (cm)	20.6	22.2	18.7	20.3

Inverse kinematics

Inverse kinematics refers to the process of determining the joint angles that are required to place an end effector at a specified point in space. Inverse kinematic analysis of the arm is calculated using a geometric method described by Korein[19] for a four degree of freedom arm. The inverse kinematics analysis was carried out for a three-dimensional mesh of points, evenly spaced 6.2 cm apart, representing proposed hand positions.

The 4 degree of freedom arm is shown in Figure 35. Points S, E, and W represent the shoulder, elbow, and wrist joint locations. Coordinates are centered on point S, which is at the center of the right shoulder, and coordinate directions are defined in relation to the torso. The z axis points down, the y axis points forward, and the x axis points to the left.

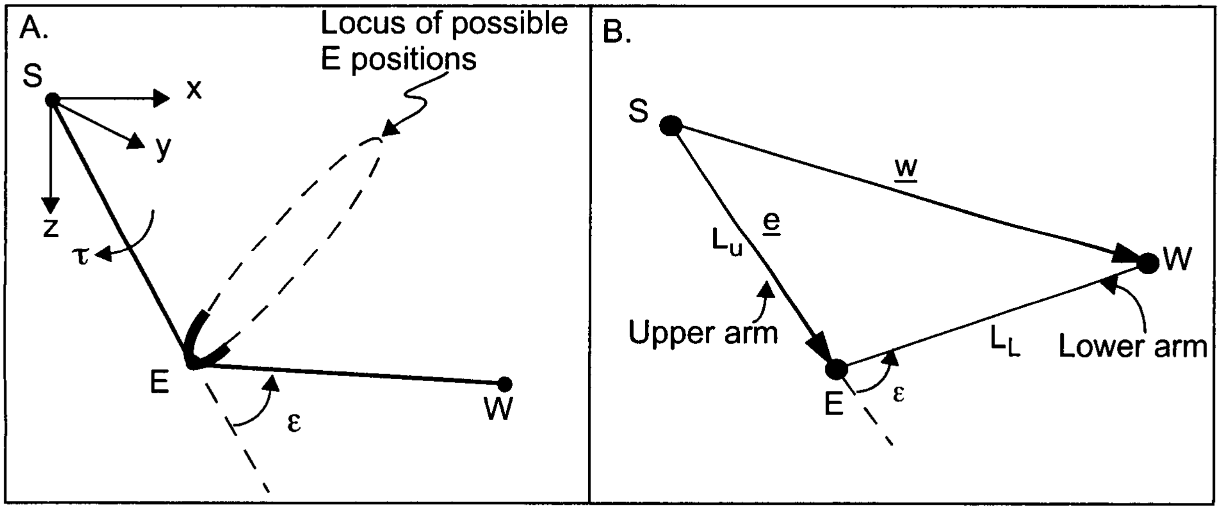

FIGURE 35. A.Two-link arm, showing the shoulder (S), elbow (E) and wrist (W) locations. B. Planar view of two-link arm.

The hand target position uniquely determines the elbow angle, while coordinated displacements of the shoulder flexion, shoulder abduction, and humerus rotation joints allow the arm to assume multiple configurations that all place the hand on the target. If 360 deg rotation of all joints were allowed, the locus of possible elbow positions that place the hand on target would be the dashed circle shown in Figure 35A. Since the joint ranges are limited, the elbow position locus forms arcs on the circle, like the solid arc in Figure 35A. In virtually all cases, there are many possible arm configurations that place the hand at its target position.

The following procedure, adapted from Korein's[19] human arm inverse kinematics method, is used to determine if a proposed hand target point W lies within the arm reach space and calculate the shoulder flexion, shoulder abduction, humerus rotation and elbow flexion angles required to place the hand at the target position. Rot($\underline{x}$,θ) indicates the rotation matrix required to rotate a vector about an axis described by vector $\underline{x}$ by angle θ.[15]

1. Determine the elbow angle ε.

The elbow angle ε is determined uniquely by the distance between the shoulder joint and the hand target point, $|\underline{w}|$. Based on $|\underline{w}|$ and the lengths of the upper and lower arm L_u and L_l, ε is calculated from the law of cosines, as shown in Figure B and Equation 26.

$$\varepsilon = \pi - \mathrm{acos}\left[\frac{(L_u^2 + L_L^2 - |\underline{w}|^2)}{2L_uL_L}\right] \qquad \text{Eq 26}$$

The hand position $\underline{w}_1$ that results from the elbow joint rotation alone is determined by 27. The hand position $\underline{w}_1$ is a three-element vector in the coordinate frame given in Figure 35A.

$$\underline{w}_1 = L_u\begin{bmatrix}0\\0\\1\end{bmatrix} + L_L\begin{bmatrix}\sin(\pi-\varepsilon)\\0\\-\cos(\pi-\varepsilon)\end{bmatrix} \qquad \text{Eq 27}$$

2. Prescribe a humerus rotation angle, τ.

A range of humerus rotation angles, τ, distributed evenly over the available humerus rotation range, -113 deg to 70 deg, is chosen. The hand position that results from each of the humerus rotation angles is then calculated.

$$\underline{w}_2 = \mathrm{Rot}(\underline{z},\tau)\underline{w}_1 \qquad \text{Eq 28}$$

Any choice of τ that results in permissible values for the other three arm joint angles (shoulder flexion, shoulder abduction, and humerus rotation) is an allowed arm configuration. To resolve the kinematic redundancy, the inverse kinematics calculations were carried out in parallel for multiple values of τ, then one arm configuration was chosen to minimize the torques required at the joints to maintain the arm configuration.

3. Rotate the shoulder to bring $\underline{w}_2$ to $\underline{w}$, without changing the humerus rotation angle.

The shoulder flexion and shoulder abduction rotations are performed simultaneously by rotating vector $\underline{w}_2$ about the shoulder so that the hand moves to its target location. In order to preserve the τ specified in step 2, the rotation axis must be chosen to avoid rotations about the z axis. The rotation axis must also be equidistant from $\underline{w}_2$ and $\underline{w}$, in order to rotate $\underline{w}_2$ to $\underline{w}$. The unit vector in the x-y plane that is equidistant from $\underline{w}_2$ and $\underline{w}$ is defined as $\hat{\underline{a}}$ and is given by:

$$\hat{\underline{a}} = \frac{\begin{bmatrix}(w_y - w_{y2})\\-(w_x - w_{x2})\\0\end{bmatrix}}{\left\|\begin{bmatrix}(w_y - w_{y2})\\(w_x - w_{x2})\\0\end{bmatrix}\right\|}. \qquad \text{Eq 29}$$

The shoulder rotation angle required, η, is the angle between the projections of $\underline{w}_2$ and $\underline{w}$ on the plane perpendicular to $\hat{\underline{a}}$. To determine η, the projections of $\underline{w}_2$ and $\underline{w}$ on the plane perpendicular to $\hat{\underline{a}}$ are defined as follows.

$$\begin{aligned}\underline{pw} &= (\hat{\underline{a}} \times \hat{\underline{w}}) \times \hat{\underline{a}}\\ \underline{pw}_2 &= (\hat{\underline{a}} \times \hat{\underline{w}}_2) \times \hat{\underline{a}}\end{aligned} \qquad \text{Eq 30}$$

The angle between $\underline{pw}$ and $\underline{pw}_2$ determines η.

$$\eta = \mathrm{acos}\left[\frac{\underline{pw} \bullet \underline{pw}_2}{|\underline{pw}||\underline{pw}_2|}\right] \qquad \text{Eq 31}$$

Since the numerator and denominator in Equation 31 are both always positive, the sign of η is determined according to Equation 32, so that the rotation is right-handed with $\hat{\underline{a}}$.

$$\begin{aligned}&\eta > 0, \underline{w} \times \underline{w}_2 \bullet \hat{\underline{a}} > 0\\ &\eta < 0, \underline{w} \times \underline{w}_2 \bullet \hat{\underline{a}} < 0\end{aligned} \qquad \text{Eq 32}$$

This single rotation of angle η about axis $\hat{\underline{a}}$ will later be decomposed into shoulder flexion and shoulder abduction angles.

4. Determine the elbow position.

The new elbow position $\underline{e}_1$ that results from the shoulder rotation is determined by rotating the vector from point S to point E by angle η about axis $\hat{\underline{a}}$.

$$\underline{e}_1 = \underline{e}\mathrm{Rot}(\hat{\underline{a}}, \eta) \qquad \text{Eq 33}$$

5. Determine the shoulder flexion and shoulder abduction angles.

The shoulder flexion and shoulder abduction angles can be determined by the vector from the shoulder S to the elbow $\underline{e}_1$. The shoulder flexion and shoulder abduction degrees of freedom are assumed to be successive rotations about perpendicular axes. The shoulder flexion (SF) rotation, which is performed first, is a rotation about the negative x axis. The shoulder abduction (SA) rotation, performed second, is a rotation about the a negative y axis that is attached to the upper arm segment and rotated with the shoulder flexion rotation. While the order of the two shoulder rotations must be specified and applied uniformly, there is no inherently preferred ordering.

$$\mathrm{SF} = \mathrm{atan}\left(\frac{e_{1y}}{e_{1z}}\right) \qquad \mathrm{SA} = \begin{cases} \mathrm{atan}\left(\frac{e_{1x}}{e_{1y}}\sin(\mathrm{SF})\right), \ \mathrm{SF} \neq 0 \\ \mathrm{atan}\left(\frac{e_{1x}}{e_{1y}}\right), \ \mathrm{SF} = 0 \end{cases} \qquad \text{Eq 34}$$

At this point in the procedure, angles for the four arm joints have been calculated for ten arm configurations corresponding to the ten prescribed values of humerus rotation angle. All of these arm configurations place the hand on the target, although some of them are unattainable because they exceed the available joint ranges of motion. The space suit model is used next to determine the torque required to maintain each of these arm configurations. A single arm configuration is then chosen as a unique solution, based on the torques needed to hold the configuration.

Space suit joint torques

Torques required to hold the space suit in the configurations determined by the inverse kinematics analysis were calculated from the regression model given in Equation 25 and Table 9. Because the arm position is considered to be static in the work envelope configuration, the angular velocity term in Equation 25 is set to zero, to isolate the torque needed to hold a specific joint angle.

Reach difficulty metric

The difficulty of reaching a specific location is indicated by the reach difficulty metric, which is a nondimensional, positive scalar corresponding to each proposed arm configuration. A low reach difficulty metric means that the arm configuration is easy to maintain; a high reach difficulty metric means that the arm configuration is difficult to maintain. The reach difficulty metric is the sum over three arm joints: shoulder flexion, shoulder abduction, and elbow flexion, of the required joint torque divided by either the positive or negative torque limit for that joint, as shown in Equation 35. The humerus rotation joint is not included because torque is not required to hold a static humerus rotation joint position.

$$\mathrm{metric} = \sum_{\mathrm{joint\ 1}}^{\mathrm{joint\ 3}} \left(\frac{\mathrm{torque}}{\mathrm{torque\ limit}}\right) \qquad \text{Eq 35}$$

For each proposed hand location, the inverse kinematics analysis outputs several arm configurations that place the hand at the target location. The torques required to maintain these arm configurations are compared to the torque limits. If the torque at any joint exceeds its limit, that arm configuration is eliminated from consideration. When more than one arm configuration is allowable, the one with the lowest reach difficulty metric is chosen as the single solution for that hand location. Because a single arm configuration is chosen for each proposed hand location, one value of the reach difficulty metric corresponds to each point in the proposed workspace. There are no constraints applied to the reach difficulty metric; the torque limits that determine whether a point is within the work envelope apply only to torques required from individual joints.

Boundary smoothing

The boundaries of the work envelope regions are smoothed using image processing techniques to set the simplest work envelope boundaries that include as many low-torque points as possible and exclude excessive-torque and nonvisible points. The smoothing technique chosen is objective and systematic and uses standard Matlab library functions, although other smoothing techniques may be used to accomplish similar results. A binary image is formed from a horizontal or vertical planar section of the workspace, with points in the "always include" category set to be black and points outside that category set to be white. The "always include" category is the region of points that is visible and requires no more than 15% of the maximum torque for each joint. Additional points from the "possibly include" category are added to this region, or colored black, using morphological operators to fill interior gaps in the black region. A gaussian low-pass filter is then applied to the image, resulting in a blurred, grayscale version of the image. The grayscale image is converted back to binary form, using a variable threshold value. The threshold is chosen to meet two conditions:

1. The smoothing process may add no more than 30% new points to the image
2. A piecewise linear boundary drawn around the white region in the smoothed image should require the minimum number of vertices.

The smoothing algorithm was carried out first for horizontal slices, then for vertical slices through the workspace region.

5.3 Results

Smoothed work envelope boundaries Three-dimensional plots of the work envelope boundaries that were calculated using female and male anthropometric data for 50th percentile size and 95th percentile strength are shown in Figure 36 and Figure 37.

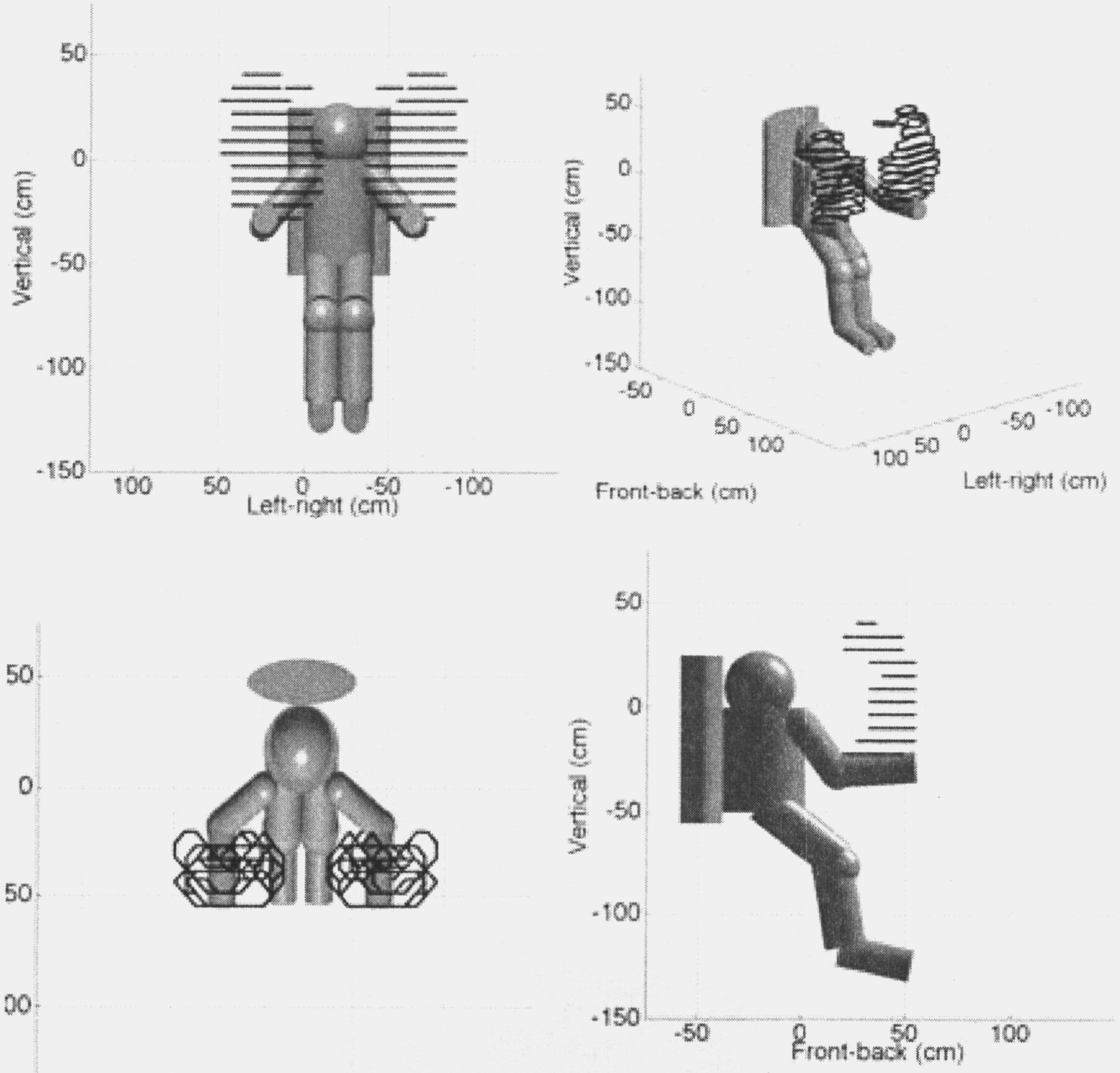

FIGURE 36. Smoothed work envelope boundaries for female, 50th percentile size, 95th percentile strength.

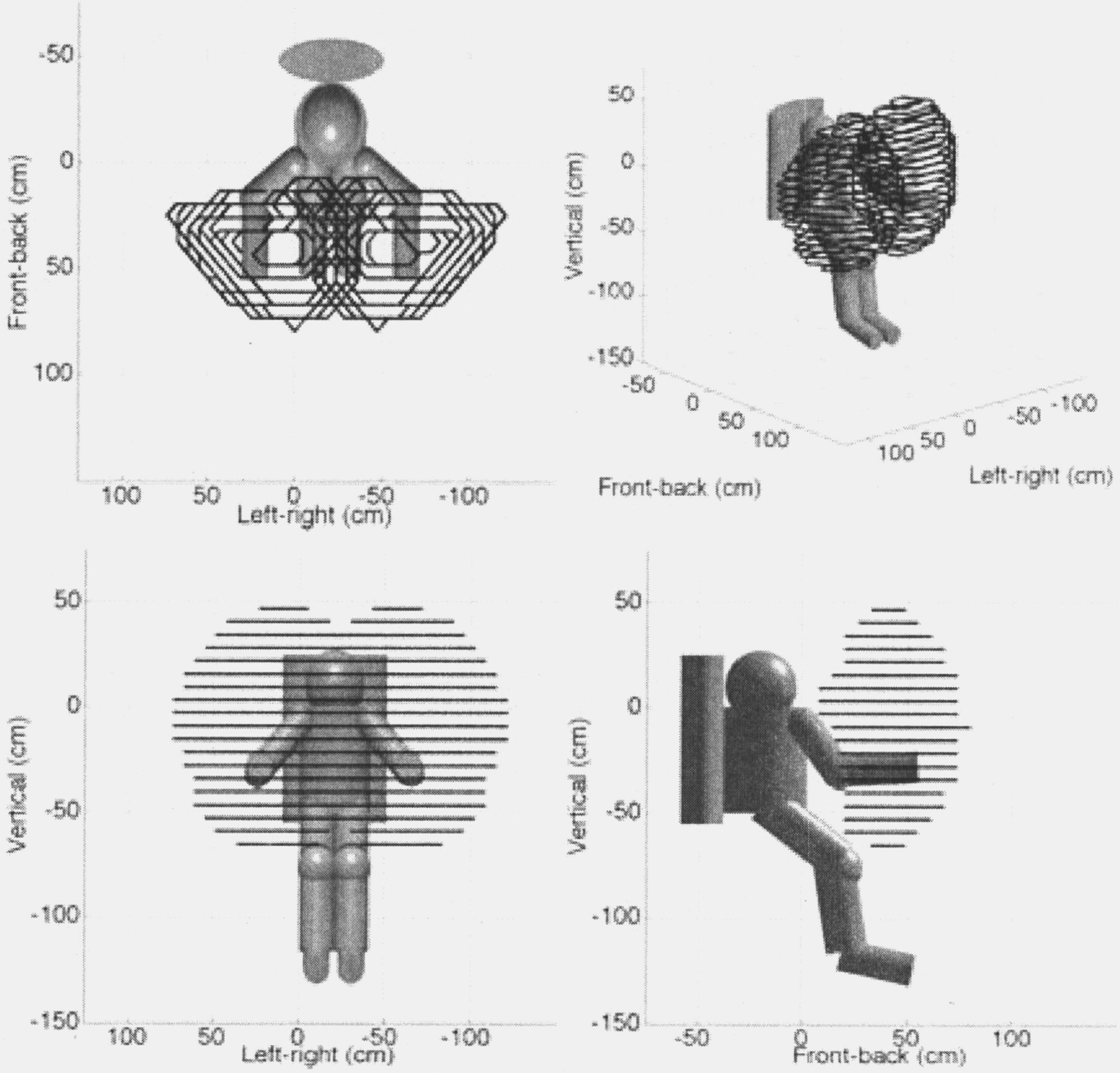

FIGURE 37. Smoothed work envelope boundaries for male, 50th percentile size, 95th percentile strength.

Horizontal slices through the work area, illustrating the reach difficulty metric and the smoothed work envelope boundaries are shown in Figure 38 for the female 50th percentile size, 95th percentile strength case and Figure 39, for the male, 50th percentile size, 95th percentile strength case.

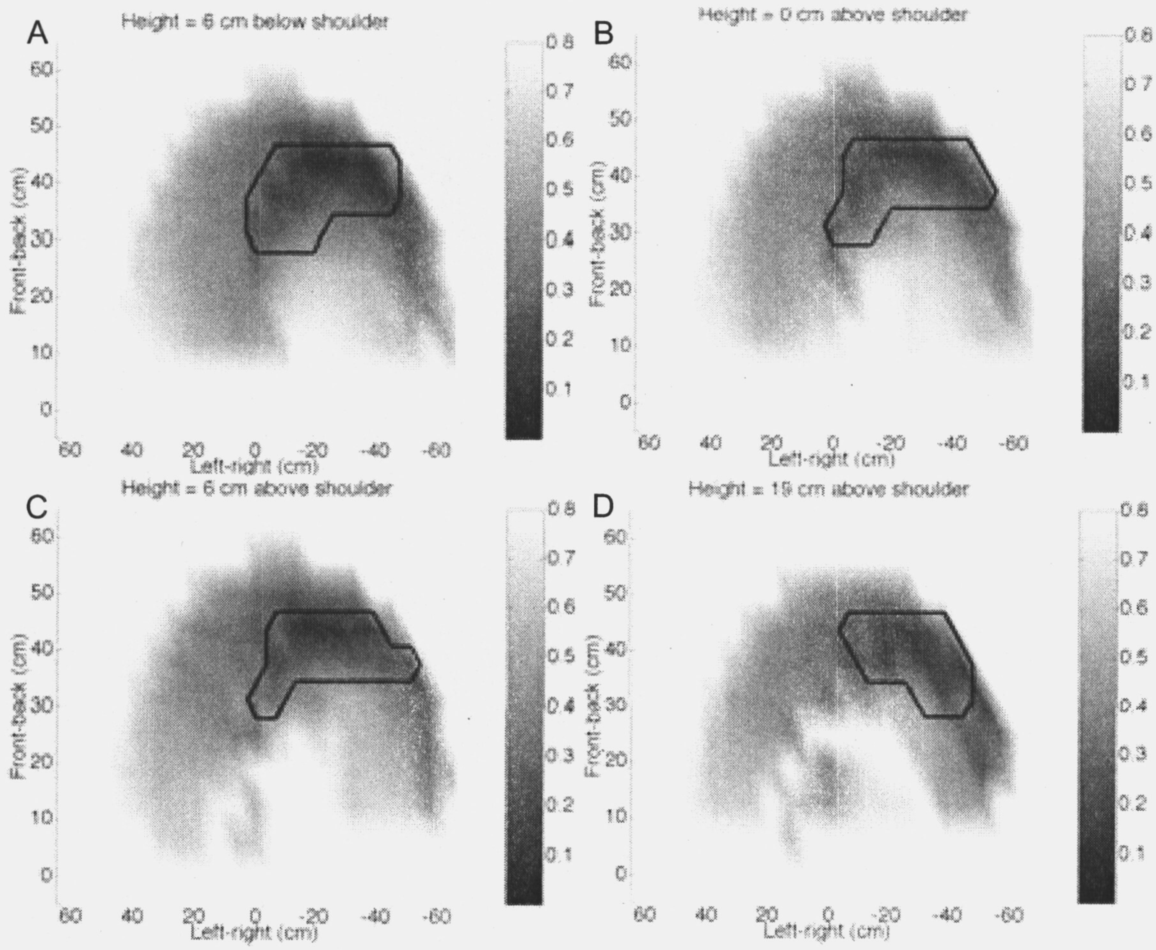

FIGURE 38. Reach difficulty metric shown by intensity and work envelope boundaries shown by black line for female, 50th percentile size and 95th percentile strength. A.) 6 cm below shoulder. B.) At shoulder level. C.) 6 cm above shoulder. D.) 19 cm above shoulder.

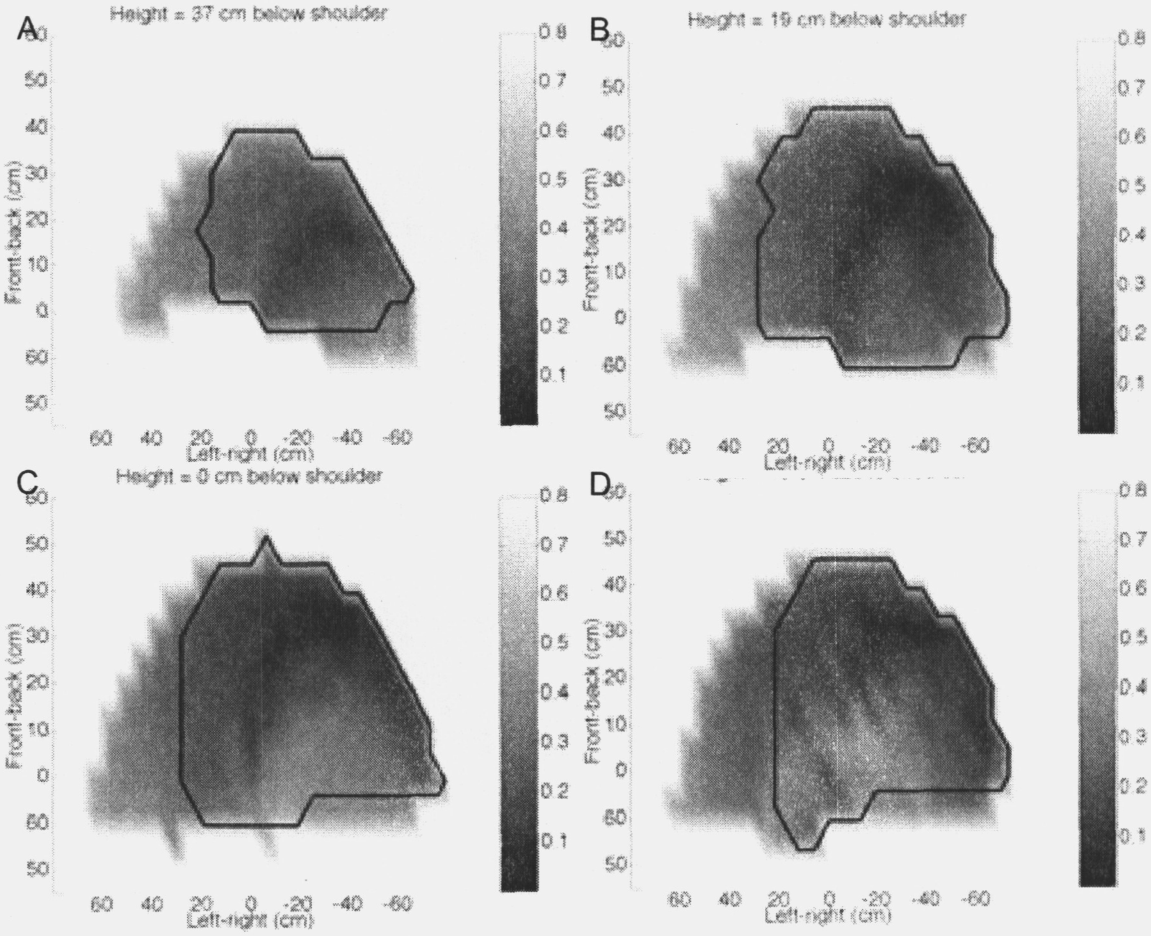

FIGURE 39. Reach difficulty metric shown by intensity and work envelope boundaries shown by black line for male, 50th percentile size and 95th percentile strength.A.) 37 cm below shoulder. B). 19 cm below shoulder. C.) At shoulder level. D.)19 cm above shoulder.

Joint angle ranges The space suit torque model, arm segment lengths, and joint torque limits determine the angle range that is generated by the work envelope analysis for each joint. Ranges of motion of each of the four arm joints for torque limits of 15%, 30%, 50% and 100% of the maximum isometric strength are shown in Figure and Figure . These ranges of motion are the maximum and minimum joint angles selected in the inverse kinematics analysis. While they do span the majority of available joint angles, they are not mathematically guaranteed to cover the entire range of feasible joint angles predicted by the space suit torque model and the strength limits. Consequently, small numerical differences can be seen between the angle ranges for cases that have the same strength limits but different arm lengths.

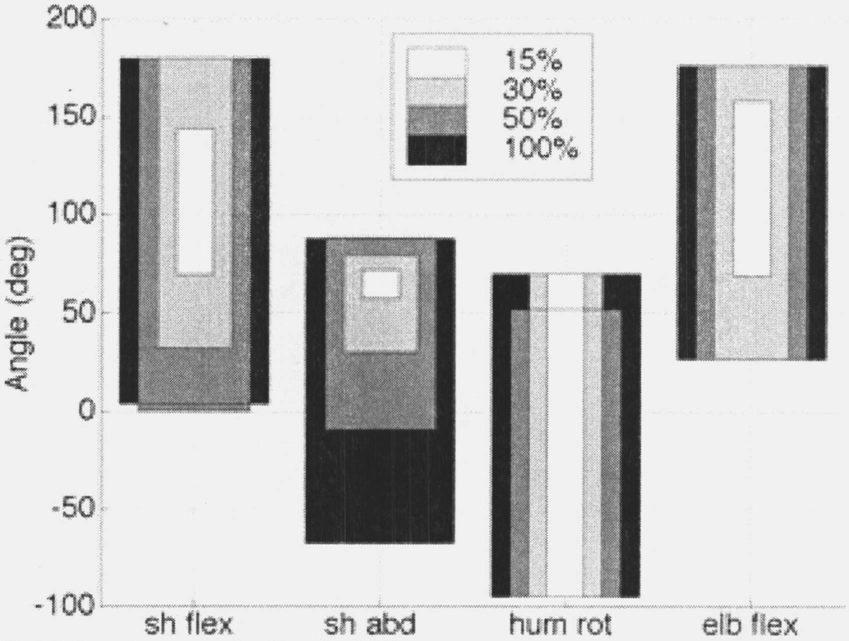

FIGURE 40. Joint angle ranges for female, 50th percentile size, 95th percentile strength deduced from work envelope analysis.

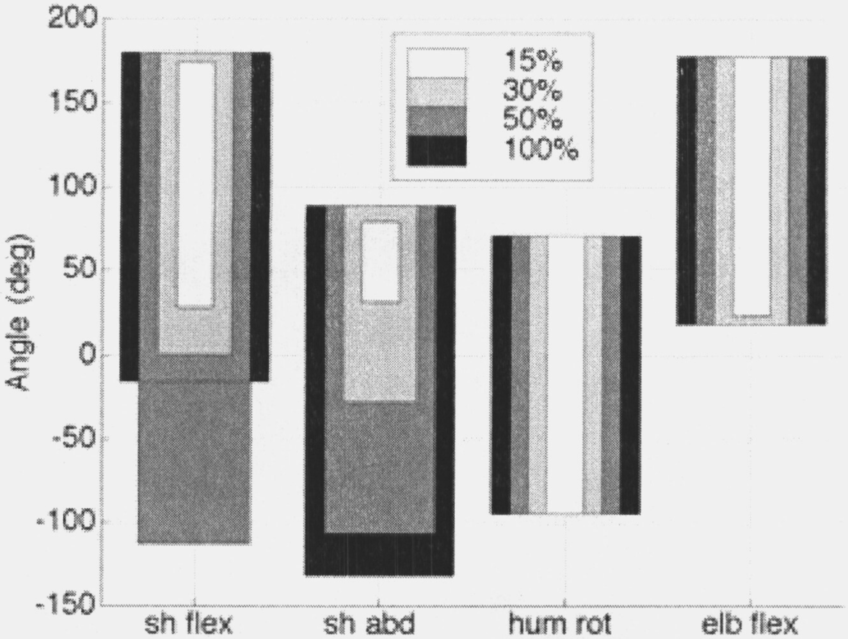

FIGURE 41. Joint angle ranges for male, 50th percentile size, 95th percentile strength deduced from work envelope analysis.

Work envelope volume The volume enclosed within the work envelope boundaries serves as one global measure of work envelope size, for purposes of comparison. The cases tested in the work envelope analysis produced different volumes for the boundaries enclosing the 15%, 30%, 50% and 100% strength contours. Volumes enclosed by these boundaries are shown in

Figure 42. Work envelope volume is shown in Figure 43, normalized by the volume of a hemisphere whose radius is equal to the arm length for the particular case tested.

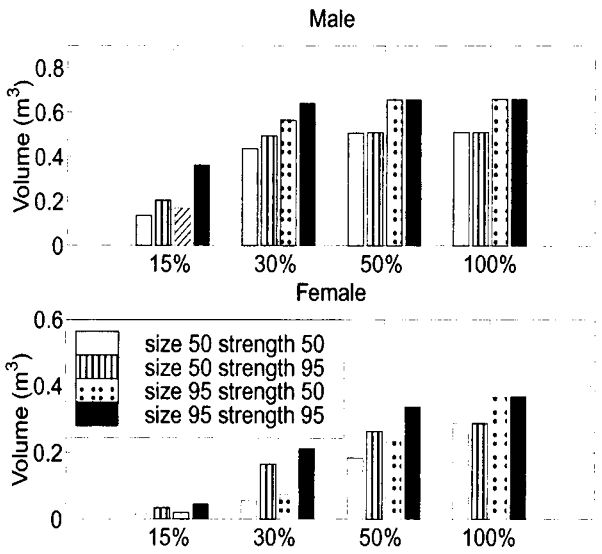

FIGURE 42. Volume enclosed within the 15%, 30%, 50%, and 100% torque limit boundaries for different anthropometric conditions.

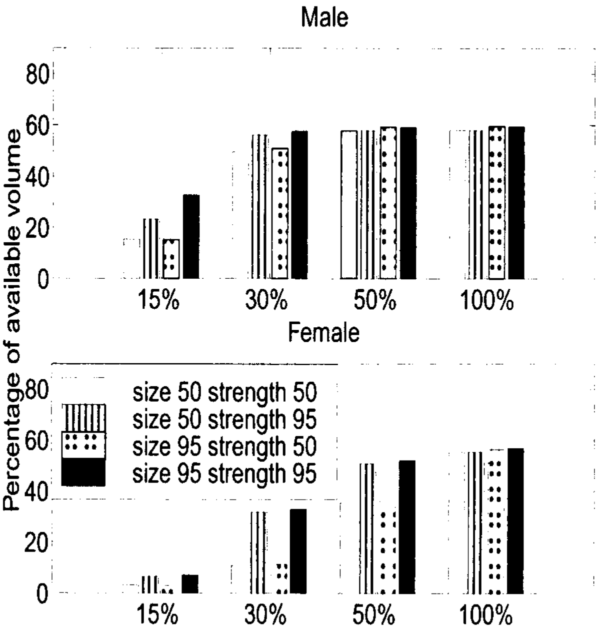

FIGURE 43. Volume enclosed within the 15%, 30%, 50%, and 100% torque limit boundaries for different anthropometric conditions, normalized by available volume.

Sensitivity analysis

The three work envelope criteria, torque limits, visibility, and boundary shape, contribute to the size and shape of the work envelope. Because multiple constraints set the boundaries of the work envelope, it is informative to determine which constraints affect the outcome of the work envelope analysis and which constraints do not. The combination of space suit joint stiffness and human strength limits sets the range of motion for each joint. The joint ranges of motion, combined with the lengths of the arm segments, determine the region that a person can reach. In addition, visibility limits may exclude reachable but out of view areas from the work envelope. Using anthropometric data that represents the size and strength of real people makes the relationship between the work envelope criteria and the resulting work envelope more complicated. For instance, increasing a high, but realistic, torque limit may not increase the size of the work envelope if the joint can already traverse its full range with the lower torque limit. The results of the sensitivity analysis illustrate how the astronaut's size, strength and visibility and the space suit's stiffness affect the size and shape of the work envelope.

Human body size Body size enters the inverse kinematics analysis through the lengths of the upper and lower arm segments. The joint angle ranges of motion shown in Figure 40-Figure 41 indicate that body size had only a very small effect on the ranges of motion of the joints. The small changes that are seen in joint ranges of motion between 50th percentile size and 95th percentile size people occur because the inverse kinematics analysis does not guarantee use of all of the available range of the joints. Because changing the arm segment lengths changes the required joint angles for a given hand position, it is expected that the joint angles output from the inverse kinematics analysis will be slightly different for different arm lengths.

The work envelope volume, plotted in Figure 42, and the percentage of available volume occupied by the work envelope, shown in Figure 43, give an overall picture of the work envelope size. At the 50% and 100% torque limits for the male anthropometric data and the female 95th percentile strength anthropometric data, the work envelope volume is determined solely by the arm length. The dominant effect of arm length on work envelope volume at the female 95th percentile strength and male 50% and 100% torque limits can be seen in Figure 43, where the percentage of available volume occupied by the work envelope is virtually the same in all cases. The uniformity of work envelope volumes for the male, 50% and 100% torque limits is explained by Figure 41, which indicate that the joint ranges of motion for 50% and 100% torque limits vary only slightly over all four male size and strength combinations. A different trend is seen for the female, 50th percentile strength, anthropometric data, where work envelope volume consistently increases as torque limits increase.

When the torque limits are high enough that the full ranges of the joints are available, the arm length determines the work envelope volume. This is the case for the 50% and 100% male torque limits and the 50% and 100% torque limits for female, 95th percentile strength, but it is not true for the female 50th percentile strength data, because the female 50th percentile strength torque limits are lower. Both arm length and strength limits affect the work envelope size for the female 50th percentile strength anthropometric data, at all torque limit levels.

Human strength limits and space suit joint stiffness Human strength limits and the torques required to bend the space suit joints together determine the available range of motion of each joint. As the strength limits increase or the space suit joints requires less torque, the range of motion expands. Benefits associated with increasing torque limits or decreasing space suit stiffness are exhausted when the joints achieve their full range. When the full range of a joint is available, increasing torque limits further does not increase the size of the work envelope, and the work envelope size and shape are limited by the visibility constraint and arm segment lengths. Changes in work envelope volume due to changes in torque limit levels (15%, 30%, 50% or 100%) and strength percentile values (50th percentile or 95th percentile) illustrate the effects of across-the-board reductions in space suit stiffness, while a more detailed analysis of the effects of increasing individual joint torque limits shows the effects of improving mobility in single joints.

Figure 43 shows the normalized volume occupied by the work envelope for 15%, 30%, 50% and 100% torque limits. For the male, 50th percentile size, 95th percentile strength case, increasing the torque limits from 15% to 30% results in an increase in work envelope volume of 270%, while increasing the torque limits further to 50% results in an additional gain in work envelope volume of only 5%. Therefore, reducing the stiffness of all space suit joints by a factor of two results in a large increase in work envelope volume, while further reductions in space suit stiffness produce little gain.

Looking at the effects of increasing torque limits for individual joints indicates which joints limit the overall size of the work envelope and where each joint's limits bound the work envelope. Individual joints were analyzed using the female, 50th percentile size, 95th percentile strength case. The baseline case uses torque limits of 30% of the maximum strength for all joints. Six variations on the baseline case were analyzed, varying the positive and negative torque limits on the shoulder flexion, shoulder abduction, and elbow flexion joints. The humerus rotation joint was not considered because the space suit's arm bearing allows it to traverse its full unsuited range of motion without reaching the 30% torque limits. In each variation evaluated in the sensitivity analysis, the positive or negative torque limit for one joint was increased from 30% of the strength limit to 50% of the strength limit. The work envelope volume in the baseline case and the six variations, normalized by the volume of a hemisphere with radius equal to the total arm length, are shown in Figure 44. The largest gain in work envelope volume is associated with an increase in the negative shoulder abduction torque limit. Increasing the negative shoulder flexion torque limit also increases the work envelope volume somewhat, while positive shoulder flexion and positive and negative elbow flexion do not limit the work envelope volume.

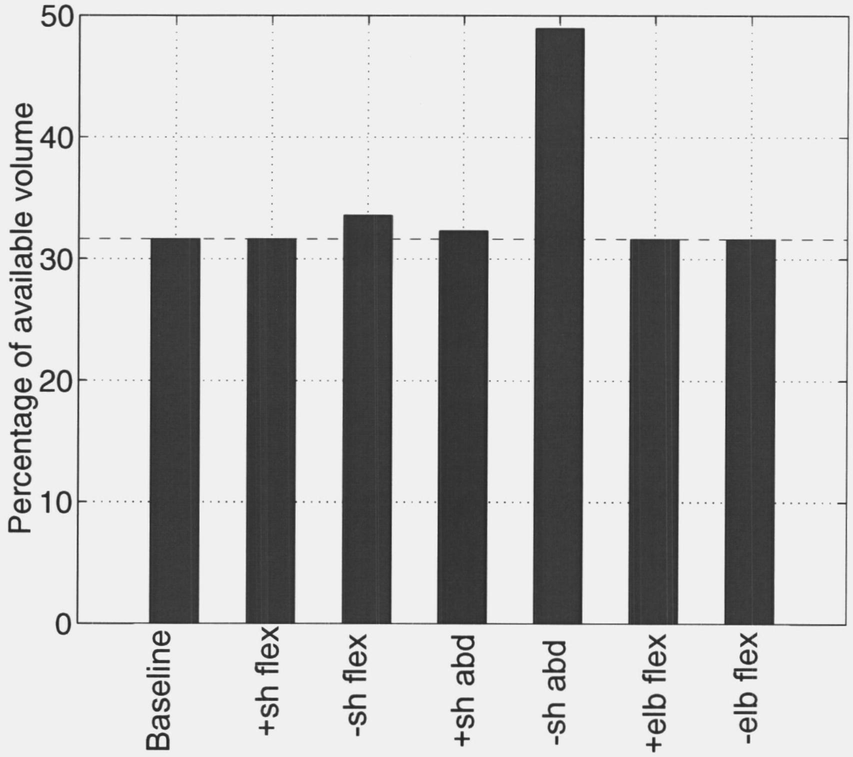

FIGURE 44. Percentage of available volume occupied by work envelope when torque limits are increased from 30% to 50% for single joints. The baseline case uses torque limits of 30% of the strength limits for all joints.

Visibility The visibility constraint excludes areas close to the body, at the top and bottom of the work space, from the work envelope. The 30% torque contours calculated using field of view restrictions were compared to boundaries calculated using the same torque limits but no field of view restrictions for male 50th percentile size, 95th percentile strength and female 50th percentile size, 95th percentile strength. As Figure 45 shows, the visibility limits exclude areas from the work envelope at the top and bottom, close to the body, but they do not change the right and left sides of the work envelope boundaries. Removing the visibility constraint increases the volume occupied by the work envelope by 33% in the male case studied and 22% in the female case.

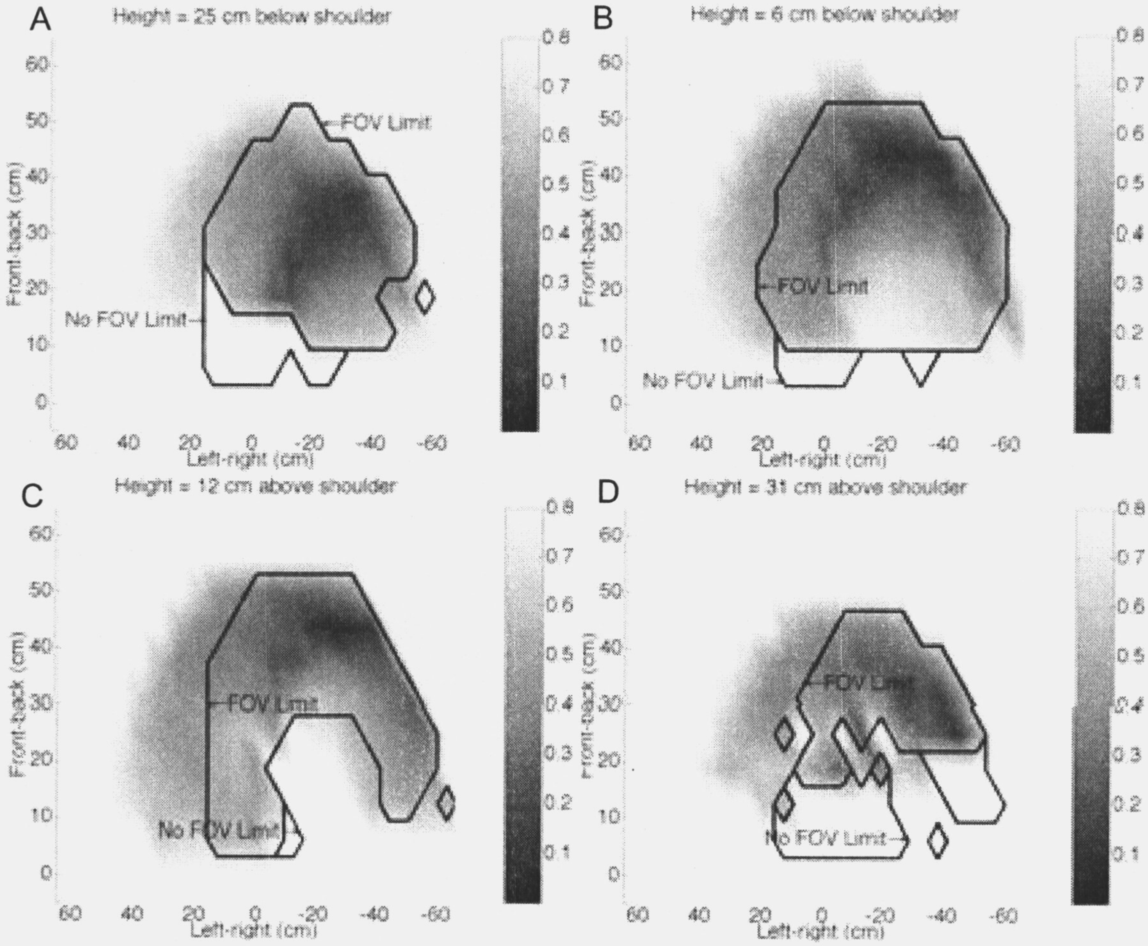

FIGURE 45. Comparison of 30% torque contours with and without visibility limits, for female, 50th percentile size, 95th percentile strength. A.) 12 cm below shoulder. B.) 19 cm above shoulder. C.) 31 cm above shoulder. D.) 44 cm above shoulder.

The work envelope analysis demonstrates the practical utility of modeling the space suit mechanics on a fundamental level, yielding both operational and design recommendations. Using models of the torque-angle relations of the space suit joints and space suit kinematics, data on visibility in the space suit, and a spatial smoothing algorithm, a rapid, systematic, and customizable method was developed to determine work envelope boundaries for a space-suited astronaut.The method was used to calculate work envelope boundaries for two cases, using both male and female anthropometric data. In addition to boundaries on suitable locations of work areas, the work envelope analysis also indicates the relative difficulty of holding the hand in different locations while wearing a space suits.

Two important simplifying assumptions were made in the analysis, which limit the numerical and statistical accuracy of the results. First, the joints of the human arm were assumed to have constant rotation axes throughout their entire range of motion, resulting in potential errors in computed hand position of approximately 1 cm-2cm. These hand position errors are within the 6.2 cm mesh spacing for trial hand positions. Second, several human body dimensions, which were obtained from anthropometric databases at the 50th percentile and 95th percentile levels, were combined in this analysis. Because the anthropometric data were combined, the work envelopes generated by the analysis should not be considered to be exact 50th percentile or 95th percentile work envelopes.

A sensitivity analysis of the work envelope boundaries, which varied joint torque limits, arm length, and visibility limits, yielded several space suit design recommendations. Increasing mobility of the space suit's shoulder joint to allow the arm to be brought closer to the body centerline in front of the body results in the largest gains in work envelope size. An across-the board reduction in space suit joint stiffness by a factor of 2 results in large gains in work envelope size, while further reductions in space suit joint stiffness only yield small gains. Visibility improvements in the upward and downward directions increase the work envelope size, while visibility does not limit work envelope size in the left and right directions.

6.0 Summary and Future EVA Research

The primary aim of this report was to summarize the research effort undertaken to advance the current understanding of astronauts' capabilities and limitations in space-suited EVA by compiling a detailed database of the torques needed to bend the joints of a space suit, developing models of the mechanics of space suit joints based on experimental data, and utilizing these models to estimate a human factors performance metric, the work envelope for space suited EVA work.

6.1 Space suit mobility database

The space suit torque-angle database was collected using an Extravehicular Mobility Unit space suit, in a novel measurement approach which used both human subjects and an instrumented robot to collect joint angle and joint torque data for realistic human motions. Human test subjects carried out arm and leg motions both wearing the space suit and not wearing the space suit, supplying realistic joint angle trajectories for each of 20 motions. The joint angle trajectories produced by the human subjects were then used as command inputs for the instrumented robot, so that the robot imitated the humans' motions while torques were measured at each of the robot's joints. Torques on the robot's joints due to the weight of the robot and space suit were subtracted from the torques that the robot measured, resulting in a consistent set of joint angle and torque data.

The database compiled in this work is more extensive than any other published space suit torque-angle data set, covering 11 joints over a large range of angles, including multiple degrees of freedom at the shoulder, hip, and ankle. Realistic, three-dimensional human-generated motions were used for data collection. Because torque data was collected by the robot as a surrogate for a human occupant of the space suit, the torques measured in this study are more representative of realistic conditions than data from previous studies[2, 7, 27] that measured joint stiffnesses for empty, pressurized space suits. A limited comparison of torques required to bend the elbow and knee to two angles, shown in Table 13, illustrates that the torques measured in this study are higher than the torques measured with empty space suits. The space suit torque-angle database serves as a basis for developing and validating both mathematical and physical models of space suit joint mobility characteristics.

TABLE 13. Space suit joint torques

Study	Dionne	Menendez et al	Abramov et al.	Morgan et al.	Current Study
Methods	EMU empty suit	Prototype joint segments, empty	Orlan-DMA, 4.3 psi (30 KPa) empty suit	EMU human subjects	EMU, human subjects and robot
Knee, 72 deg.	3.2 Nm	NA	6.0 Nm	8.1 Nm	3.74±.0676 Nm
Elbow, 80 deg	2.0 Nm	2 Nm	2.2 Nm	3.4 Nm	14.6±.136 Nm

6.2 Modeling

The space suit torque-angle database presents a rare opportunity to develop models of space suit mobility and verify them against experimental data. Models of space suit mobility are useful in two applications: first, numerically predicting the torque required to bend a space suit's joints and second, understanding the physical processes that determine the stiffness of a space suit's joints. These two applications clearly require two different modeling approaches: a descriptive mathematical modeling technique based on experimental data and a theoretical model based on physical principles. Section 4 describes two modeling efforts: a mathematical model based on empirical data that predicts the torque required to bend the space suit's joints and a comparison between two physics-based models of bending pressurized cylinders and the space suit torque angle database.

Numerical predictions of the torque required to bend space suit joints were generated using a mathematical hysteresis modeling technique. The experimental data reported in Section 3, as well as other investigators' data, indicate that the torque-angle relationship for space suit joints is markedly hysteretic. The Preisach hysteresis model, which has been used to model other hysteretic mechanical systems, is used to mathematically model the torque required to bend the space suit joints as a function of bending angle history. The Preisach model coefficients were identified for the torque-angle characteristic of six of the space suit's joints: elbow flexion, hip flexion, hip abduction, knee flexion, ankle rotation and ankle flexion. In addition, a new method was developed for estimating the variance of the error in the Preisach model's torque predictions. Comparisons between the Preisach model's output and experimental data indicate that the Preisach hysteresis model accurately reproduces torques needed to bend space suit joints.

The physics-based modeling effort compares two approximate models of pressurized fabric cylinder bending to experimental data. The two models, the beam model and the membrane model represent limiting cases on the physical processes that govern space suit joint mobility. The beam model assumes that space suit joint bending occurs through elastic deformations of the space suit fabric, with no change in internal volume when joints are bent. In contrast, the membrane model assumes that the space suit fabric never stretches, and the work done to bend the space suit joint goes entirely into compressing the gas inside the space suit. Comparing these two approximate models to experimental data illustrates the relative importance of elasticity and volume loss on space suit joint mechanics and indicates whether the space suit behavior can be approximated by one model or the other. Understanding the physical processes that govern space suit joint performance leads to insights into how space suit joints would perform if their construction or operating conditions were changed.

Comparisons between the two models and experimental data show that the membrane model matches the elbow and knee joint torque-angle data well over a bending angle range 30-50 degrees from the equilibrium bending angle and underestimates the torque required to bend the space suit joints for more extreme bending angles. The beam model is inconsistent with both the magnitude and curve shape of the elbow and knee joint torque-angle data. Data from the hip abduction joint, which has no mobility features and is consequently very stiff, is consistent with the beam model, although the limited angle range of the data prevents the beam model from showing important qualitative characteristics.

Because the torque-angle performance of the space suit joints can be accounted for by changes in internal volume without stretching of the space suit fabric, the mobility of the EMU elbow and knee joints is not sensitive to changes in the material properties of the fabric. The membrane model predicts that the design parameters that affect space suit mobility are the internal pressure, radius of the space suit segment, and the pleat design that allows the joint to be bent without reducing the internal volume.

The physics-based modeling work in this thesis provides insights into the physical processes that govern space suit mobility, points out promising methods of improving space suit mobility and provides a theoretical basis for further experimentation to develop more sophisticated physics-based models of space suit mobility.

6.3 The work envelope: Applying space suit modeling to EVA operations

The work envelope analysis demonstrates the practical utility of modeling the space suit mechanics on a fundamental level, yielding both operational and design recommendations. Using models of the torque-angle relations of the space suit joints and space suit kinematics, data on visibility in the space suit, and a spatial smoothing algorithm, a rapid, systematic, and customizable method was developed to determine work envelope boundaries for a space-suited astronaut.The method was used to calculate work envelope boundaries for two cases, using both male and female anthropometric data. In addition to boundaries on suitable locations of work areas, the work envelope analysis also indicates which areas are best for workstation placement.

A sensitivity analysis of the work envelope boundaries, which varied joint torque limits, arm length, and visibility limits, yielded several space suit design recommendations. Increasing mobility of the space suit's shoulder joint to allow the arm to be brought closer to the body centerline in front of the body results in the largest gains in work envelope size. An across-the board reduction in space suit joint stiffness by a factor of 2 results in large gains in work envelope size, while further reductions in space suit joint stiffness only yield small gains. Visibility improvements in the upward and downward directions increase the work envelope size, while visibility does not limit work envelope size in the left and right directions.

6.4 Recommendations for future work

Experimental work Joints in the space suit include both bending joints and rotational bearing joints, to allow motion in multiple degrees of freedom in the arm. While this thesis focuses mostly on the performance of the bending joints, experimental work to quantify the motion of the space suit shoulder segment between the two bearings in the arm, as distinguished from the joint motion of the person wearing the space suit, would lead to a better understanding of the multiple degree of freedom motion at the shoulder joint.

Future experimental work would also contribute to the physics-based modeling efforts. The membrane model, which agrees closely with experimental data for the elbow and knee, predicts that joint stiffness increases linearly with space suit pressure. This result could easily be tested by measuring joint torque vs. angle at a range of pressures. Other predictions that the membrane model makes, including inextensibility, the amount of internal volume change, and the bent shape of the space suit joint could be tested in experiments with pressurized mock-ups of individual space suit joints.

The work envelope analysis makes detailed predictions of easily-reachable locations based on body size and strength. For these predictions to have practical value, the work envelope analysis should be experimentally validated. Experimental work to validate the work envelope predictions should use arm length, viewpoint location, and static joint strength data from the test subjects to predict work envelopes tailored to those individuals. Validation of the calculated work envelope should be performed in neutral buoyancy simulation, rather than a 1-g lab environment, so that the test subjects are not required to supply additional joint torques to support the weight of the space suit's arm. Test subjects would attempt to hold one hand at pre-determined locations for several minutes and subjectively rate the difficulty of holding the hand position, as well as indicating whether the point is visible. Testing points should be chosen to fall both inside and outside of the calculated work envelope, with particular attention paid to points that are inside the calculated work envelope but outside of the NASA work envelope. Data collected should include whether the subject was successful in holding the hand at the test point for the required duration, the length of time that the test subject was able to maintain the required hand position, the subjective difficulty ratings and whether the point was visible. This information should then be compared to the calculated work envelope's boundaries, the reach difficulty metric, and the visibility predictions. Modifications to the computational work envelope based on these evaluations may include changes to the percentages of maximum torque that are used as torque limits and more detailed visibility information.

Analysis Future analytical work should include implementation of existing space suit models and development of new models, based on experimental data. We have previously demonstrated in simulations that torques induced by the space suit have an important impact on body positions and loads when astronauts move large objects in EVA[30],[31]. Future EVA dynamic simulation studies should include the torques needed to bend the space suit joints established under this research effort.

New, physics-based models of space suit joint mobility should address joint design issues by including details of space suit joint construction. Work should also be done to asses the proper way of relaxing the inextensibility constraint of the membrane model to include the limited fabric stretching that likely occurs when space suit joints are bent. Hysteresis in fabrics is generally thought to be caused by the fabric threads sliding over each other as the fabric stretches[13]. Although the space suit joints show significant hysteresis, implying that there is some internal relative motion in the fabric, the membrane model's agreement with experimental data implies the contrary, that the space suit fabric is inextensible. It would be particularly interesting to account for the hysteresis mechanism in light of this apparent contradiction.

EVA standards and requirements The NSTS-07700 EVA requirements document[1] specifies NASA's requirements for the space suited work envelope and the field of view for an EVA astronaut (Figure 34). The current requirements are simply stated, requiring 4 numbers for the work envelope (3 coordinates of cylinder center location and cylinder diameter) and 5 numbers for the field of view (angular field of view in 5 directions). The simple requirements are easy to understand and visualize, lending themselves to qualitative evaluation and application to worksite design. However, much more powerful methods, including CAD modeling, are currently available for EVA worksite analysis and have the capability to enforce complicated requirements quantitatively.[3, 13] Now that advanced techniques exist for evaluating work envelope and visibility requirements, the work envelope and visibility standards should be updated to a higher accuracy and level of detail.

The work envelope standard in NSTS-07700 is significantly smaller than the work envelope calculated based on space suit mobility and human strength limits. In particular, there are large areas beyond the left and right boundaries of the NSTS-07700 work envelope that are inside the calculated work envelope. Also, a visibility analysis of the NSTS-07700 work envelope using the visibility requirements from the same standards document indicates that a portion of the NSTS-0770 work envelope is not visible. These disagreements should spur a re-evaluation of the NSTS-07700 work envelope, including visibility, body size differences, and, at the least, enlarging its left-right dimension.

The visibility standard in NSTS-07700 specifies the angular field of view in 5 directions. The lack of spatial resolution prevents this guideline from accurately specifying the visibility limitations caused by the shape of the helmet and visors and the geometry of other obstructions, including the space suit's Display and Control Module (DCM), and the mini-workstation, which both block downward visibility. Since powerful analytical techniques currently exist for assessing adherence to these requirements, the visibility requirement should be updated to improve its accuracy and make full use of the available analytical techniques for assessing compliance to requirements.

6.5 Applications to current EVA

The analytical techniques and space suit mobility database developed in this thesis can be applied to current EVA planning, training and hardware design and future planetary EVA system design. The computational work envelope method can be used for EVA and neutral buoyancy simulation planning and EVA hardware design evaluations. A larger and more realistic work envelope estimate would make more efficient use of time and resources in EVA work than the current work envelope estimate. The mathematical model developed in this thesis is implementable in real time and suitable for incorporation into EVA dynamic simulations to evaluate large mass handling situations. The mathematical model can also be incorporated into virtual reality training to supply the space suit's contribution to the virtual reality system's force feedback. Physics-based models of space suit joint mobility will aid in designing joints for planetary space suits that have the proper combination of mobility and stability for best performance in walking, running and traversing rough terrain. An analysis combining kinematics, space suit mobility models, and human strength could be used to assess the lower body mobility of planetary space suits, relating individual joint mobility to terrain-traversing capabilities, such as the maximum height of an object that can be stepped over, aiding in requirement definition for advanced space suits. The space suit mobility database and analytical techniques that were developed in this thesis can be applied to both near-term and advanced EVA planning and design by supplying realistic benchmarks on the mobility performance of the EMU space suit and enabling designers and planners to assess practical performance measures based on small-scale, joint level mobility models.

6.6 Beyond Space Suits: Human Exploration Missions and Locomotion

This research effort was enhanced by additional efforts to understand human performance in extreme environments. An additional battery of experimental tests was run. Specifically,

1. The instrumented robot space suit tester was suited in a Shuttle EMU and commanded to perform single and multiple joint motions in order to collect data that will be used to expand the joint angle and torque database as well as verify the mathematical and physical models.
    - Suited test subjects performed representative EVA tasks. A Motionstar Flock of Birds motion tracking system measured arm and leg joint positions and angles. Heart rate and surface pressure on the left thigh were also recorded. The tasks performed were focused around studying range of motion limits as well as locomotion. Tasks included:
    - Walking on treadmill at two different suit pressures
    - Arm reach (including a low reach test)
    - Foot locus with and with handhold
    - Task board

With better understanding of astronaut performance we can look ahead to future missions and propose both improvements to the current space suit as well as revolutionary new designs for partial gravity locomotion space suits. This ongoing research is aimed at radical advances in our ability to understand, simulate, and predict capabilities of suited astronauts in a variety of scenarios.

As part of the foot locus test subjects were instructed to make an upward spiral motion with their foot, both with and without a handhold. The Range of motion with the handhold was significantly greater than without. This result demonstrates the effect of balance on lower body mobility and suggests that an assisting device such as a walking stick should be utilized for human exploration missions (See Figure below).

Walking tests showed that subjects walked with longer steps and a lower stride frequency at lower suit pressures, giving a quantitative measure of the effect of suit pressure on locomotion. Stride frequencies were approximately 63 strides/min for 13.8 kPa (2 psi) and 70 strides/min for 29.6 kPa (4.3 psi).

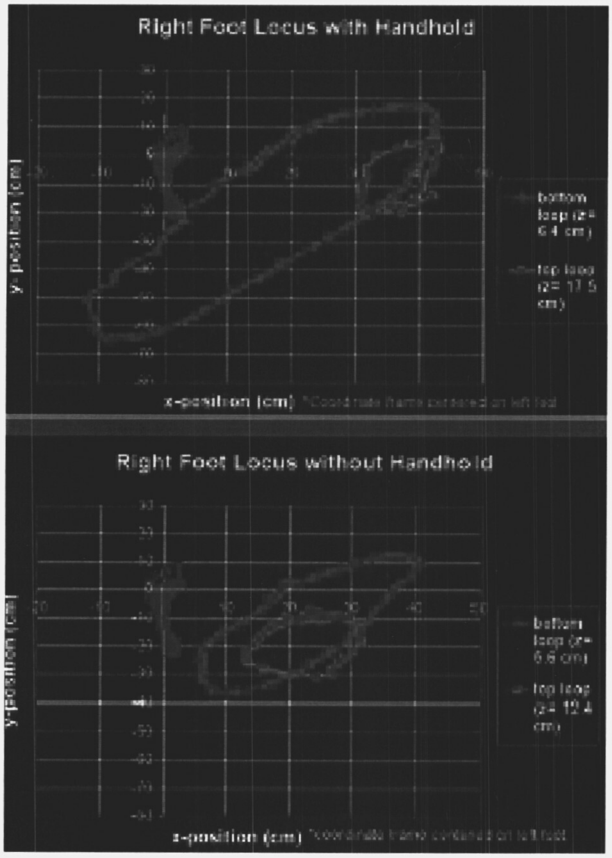

Funded under the NASA Institute for Advanced Concepts (NIAC), research efforts were extended to a new conceptual design for a space exploration system. A *Bio-Suit* System stands to revolutionize human space exploration by providing enhanced astronaut extravehicular activity (EVA) locomotion and life support based on the concept of providing a 'second skin' capability for astronaut performance[11]. The novel design concept is realized through symbiotic relationships in the areas of wearable technologies; information systems and evolutionary space systems design; and biomedical breakthroughs in skin replacement and materials. By working at the intersection of engineering; design; medicine; and operations, new emergent capabilities could be achieved. The Bio-Suit System would provide life support through mechanical counter-pressure where pressure is applied to the entire body through a tight-fitting suit with a helmet for the head. Wearable technologies will be embedded in the Bio-Suit layers and the outer layer might be recyclable. Hence, images of 'spraying on' the inner layer of the Bio-Suit System emerge, which offers design advantages for extreme, dusty, planetary environments. Flexible space system design methods are slated to enable adaptation of Bio-Suit hardware and software elements in the context of changing mission requirements. Reliability can be assured through dependence of Bio-Suit layers acting on local needs and conditions through self-repair at localized sites while preserving overall system integrity. The Bio-Suit System is relevant to NASA's strategic plan and stated visionary challenges in the Human Exploration and Development of Space, AeroSpace Technology, and Space Science enterprises.

The images below depict an astronaut wearing a mechanical counter-pressure (MCP) suit outfitted for extreme Martian exploration. A 'skin suit' layer is complemented with climbing gear, communications, biosensors, and wearable computers for duty that requires high-slope traverses, repelling, and investigating craters. An astronaut on Mars is depicted donning the comfortable elastic bio-suit layer (1). The hard torso shell (4) is donned next and seals with couplings at the hips and shoulders. The hard backpack, or portable life support system, (5) attaches mechanically to the hard torso shell, and provides gas counter pressure. Gas pressure flows freely into the helmet (2) and down tubes on the elastic bio-suit layer to the gloves and boots (3). The bio-suit layer is lightweight and easy to don and doff. It is custom fitted to each astronaut using a laser scanning/electrospinlacing process (Natick Soldier Center). Remaining suit elements are simple, functional, interchangeable and easy to maintain and repair.

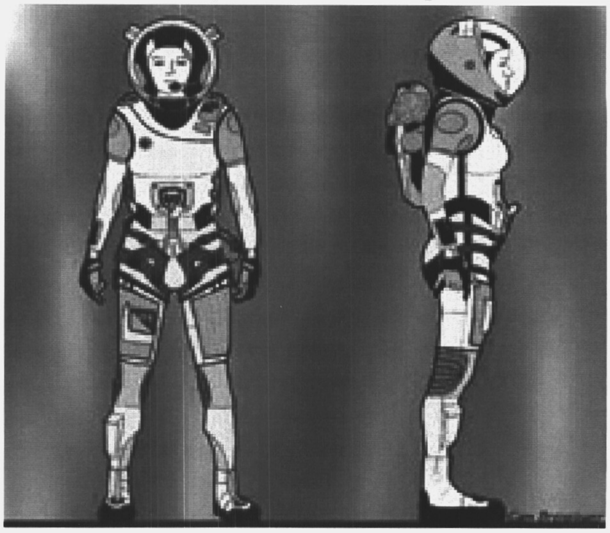

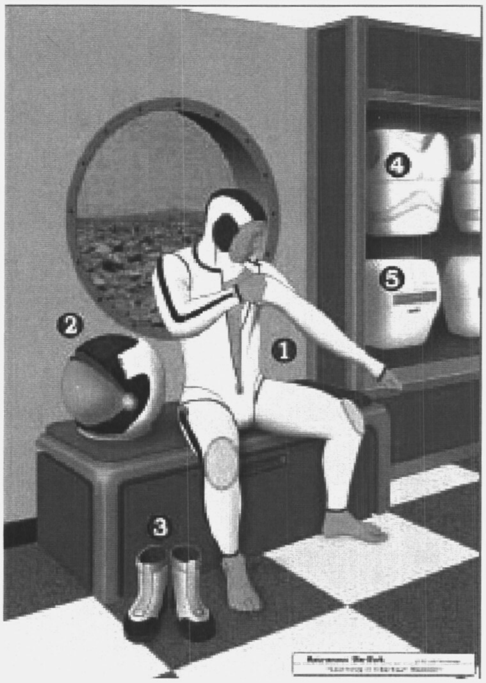

Maintenance of a windmill within the Martian colony. Harvesting power from the Martian environment will be key to the success of Martian outposts such as this. In this vision we imagine windmills as one component of the power generation hardware. Here an individual scales a windmill for regular maintenance tasks. Activities such as this push conventional space suit design to the limit, but this task feels natural while wearing the Bio-Suit. This is because of its low bulk and MCP technologies which facilitate full range of motion as well as tactile feedback from the environment. Also, integrated into the Bio-Suit are components that allow attachment of such safety devices such as the Martian prussic (shown) or other scaling/repelling equipment. This facilitates the large range of activities required of the explorers on the surface of Mars.

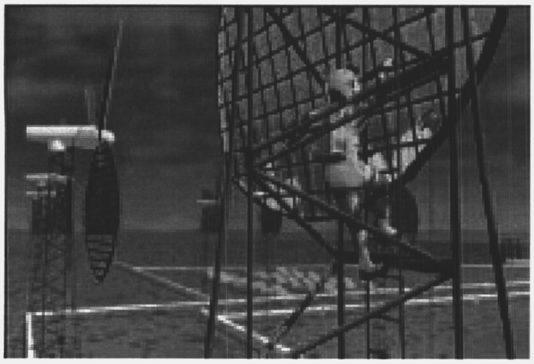

Advanced Technologies Melt blowing involves liquefying polymer and blowing it onto surfaces. It does not produce such fibrous material as electrospinlacing, but is good for creating thin elastic layers. Both melt blowing and electrospinlacing processes, but especially melt blowing, have been used in limited applications, commercially. Application can be made directly to the skin as shown here, or to advanced 3D forms generated by laser scanning. Wearable computers, smart gels and conductive materials could be embedded between polymer layers. In the illustration, melt blown gel is used to create a seamless MCP layer over the entire body. A shower-like spray device could be potentially used for suit self-application.

Electrospinlacing is a process by which a multi-filament fiber of polymer can be projected onto a grounded surface. This is achieved by charging a suspended drop of polymer with tens of thousands of volts. At a characteristic voltage the droplet forms a Taylor cone, and a fine jet of polymer releases from the surface in response to the tensile forces generated by interaction of an applied electric field with the electrical charge carried by the jet. The projected polymer can be collected as a continuous web of fibers in a range of thicknesses. Application can be made directly to the skin as shown above, or to advanced 3D forms generated by laser scanning. Wearable computers, smart gels and conductive materials could be embedded between polymer layers. In the illustration, electrostrictive gel is used to create a seamless MCP layer.

This section introduced some related, but further reaching research efforts to enhance ongoing EVA studies. All illustrations in this section drawn by Cam Bresinger.

6.7 Summary of contributions

This research effort advances current knowledge of astronauts' capabilities and limitations in space-suited EVA in three areas: by gathering data on the torques needed to bend space suit joints, developing both mathematical and physics-based models relating joint torques to angles, and using the joint torque-angle data to predict and analyze the work envelope of a space suited astronaut.

The space suit torque-angle database compiled in this thesis is more extensive in the number of joints and angular range than any other published space suit mobility data set. Furthermore, the data was collected under realistic conditions, using joint angle trajectories that were generated by space-suited human subjects and torques measured using an instrumented robot as a surrogate for a person in the space suit. This database provides the basis for developing and validating models of space suit mobility.

The modeling work in this thesis contributes both numerical predictions of the torques needed to bend the space suit joints and insight into the physical processes that govern space suit joint mobility. Preisach hysteresis model coefficients were identified from experimental space suit torque-angle data and a new method was developed for estimating the variance of the error in the Preisach model's torque predictions. The Preisach model was then used to generate numerical predictions of the torque needed to bend the space suit joint as a function of time. The physics-based modeling work compared two approximate models which describe pressurized fabric cylinder bending to experimental data. The beam model assumes that space suit joint bending occurs through elastic deformations of the space suit fabric, while the membrane model assumes that space suit fabric never stretches. The experimental data agrees most closely with the membrane model, indicating that elasticity is not an important contribution to space suit joint bending performance and efforts to improve space suit joint mobility should focus on geometrical aspects of joint design, rather than the material properties of the fabric.

The work envelope analysis demonstrates the usefulness of modeling space suit mobility in predicting a global human factors metric. The work envelope prediction method that this thesis developed is rapid and easily reconfigurable for people of different sizes and strengths. It generates not only boundaries on acceptable work sites, but also predicts the locations of desirable work sites. A sensitivity analysis on the work envelope revealed that improvements in shoulder mobility and upward and downward visibility would be most effective in enlarging the space suited astronaut's work envelope.

Concepts for a *Bio-Suit* System were introduced to show the revolutionary potential for human space exploration. These concepts enhance astronaut extravehicular activity (EVA) locomotion and life support by providing a 'second skin' capability, or mechanical counter pressure for astronaut performance in extreme environments.

7.0 References

1. "Space Shuttle System Payload Accommodations, NSTS 07700," NASA, 1988.
2. Abramov, I. P., Stoklitsky, A. Y., Barer, A. S., and Filipenkov, S. N., "Essential Aspects of Space Suit Operating Pressure Trade-off," Proceedings of the International Conference on Environmental Systems, Society of Automotive Engineers, 1994.
3. Anderson, D., "EVA Worksite Analysis--Use of Computer Analysis for EVA Operations Development and Execution," Acta Astronautica, Vol. 44, No. 7-12, 1999, pp. 593-606.
4. Astrand, P. Textbook of Work Physiology: Physiological Bases of Exercise, McGraw-Hill, New York, 1977.
5. Chaffin, DB. Occupational Biomechanics, Wiley, New York, 1984.

6. Comer, RL and Levy, S, "Deflections of an inflated circular cylindrical cantilever beam," AIAA Journal, Vol 1, No 7, July, 1963, pp. 1652-1655.

7. Dionne, S., "AX-5, Mk III, and Shuttle Space Suit Comparison Test Summary," NASA, Moffett Field, CA, EVA Technical Document 91-SAE/ SD-004, August, 1991.

8. Doong, T. and Mayergoyz, I. "On numerical implementations of hysteresis models" IEEE Transactions on Magnetics, Vol 21 p.1853-1855, 1985.

9. Fay, JP and Steele CR, "Forces for rolling and asymmetric pinching of pressurized cylindrical tubes" Journal of Spacecraft and Rockets, Vol. 36, No. 4, July-August 1999, pp. 531-537.

10. Fay, JP and Steele CR, "Bending and symmetric pinching of pressurized tubes", International Journal of Solids and Structures, Vol 37, 2000, pp. 6917-6931.

11. Frazer, A., Pitts, B., Schmidt, P., Hodgson, E, Newman, D.J., "Quantifying Astronaut Tasks: Robotic Technology and Future Space Suit Design", NASA Space Human Factors Conference, January 2002, Houston, Texas.

12. Ge, P. and Jouaneh, M. "Modeling hysteresis in piezoceramic actuators," Precision Engineering, Vol 17, p. 211-221, 1995.

13. Hagale, T. J. and Price, L. R., "EVA Design, Verification, and On-Orbit Operations Support Using Worksite Analysis," Proceedings of the International Conference on Environmental Systems, Society of Automotive Engineers, Toulouse, France, 2000.

14. Hearle J.W.S., Grosberg P., Backer S., Structural Mechanics of Fibers, Yarns and Fabrics Vol. 1., Wiley-Interscience, New York, 1969.

15. Hearn, D. and Baker, M. P., Computer Graphics: C Version, 2nd ed., Prentice Hall, Upper Saddle River, NJ, 1997.

16. Jung, E. S. and Choe, J., "Human reach posture prediction based on psychophysical discomfort," International Journal of Industrial Ergonomics, Vol. 18, 1996, pp. 173-179.

17. Jung, E. S., Kee, D., and Chung, M. K., "Upper body reach posture prediction for ergonomic evaluation model," International Journal of Industrial Ergonomics, Vol. 16, 1995, pp. 95-107.

18. Kamper, D. G. and Rymer, W. Z., "Effects of geometric joint constraints on the selection of final arm posture during reaching: a simulation study," Experimental Brain Research, Vol. 126, 1999, pp. 134-138.

19. Korein, J. U., A Geometrical Investigation of Reach. MIT Press, Cambridge, MA, 1984.

20. Kosloski, L. D., US Space Gear: Outfitting the Astronaut, Smithsonian Institution Press, Washington, DC, 1994.

21. Krasnoselskii M, Pokrovskii, A. Systems with hysteresis. Springer-Verlag, Berlin, 1989.

22. Main, JA. Analysis and design of inflatable aerospace structures. Ph.D. Thesis, Vanderbilt University, 1993.

23. Main, J. A., Peterson, S. W., and Strauss, A. M., "Material Selection for Highly Mobile Space Suit Gloves Based on Fabric Mechanical Properties," Proceedings of the 43rd IAF Congress, International Astronautical Federation, 1993.

24. Main, J. A., Peterson, S. W., and Strauss, A. M., "Design and Structural Analysis of Highly Mobile Space Suits and Gloves," Journal of Spacecraft and Rockets, Vol. 31, No. 6, 1994, pp. 1115-1122.

25. Main, J. A., Peterson, S. W., and Strauss, A. M, "Beam-type bending of space-based inflatable structures," Journal of Aerospace Engineering, Vol 8, No 2, April, 1995, pp.120-125.

26. Mayergoyz, I. D., Mathematical Models of Hysteresis, Springer-Verlag, New York, NY, 1991.

27. Menendez, V., Diener, M., and Baez, J. M., "Performance of EVA Suit Soft Flat Pattern Mobility Joints," Proceedings of the International Conference on Environmental Systems, Society of Automotive Engineers, 1994.

28. Morgan, D. A., Wilmington, R. P., Pandya, A. K., Maida, J. C., and Demel, K. J., "Comparison of Extravehicular Mobility Unit (EMU) Suited and Unsuited Isolated Joint Strength Measurements," NASA TP-3613, Houston, TX, June, 1996.

29. NASA, "Man-Systems Integrations Standards, NASA-STD-3000," 1995.

30. Newman, D. J., Schmidt, P. B., Rahn, D. B., Badler, N., and Metaxas, D., "Modeling the Extravehicular Mobility Unit Space Suit: Physiological Implications for Extravehicular

Activity," Proceedings of the International Conference on Environmental Systems, Society of Automotive Engineers, Toulouse, France, 2000.

31. Rahn, D. B., "A Dynamic Model of the Extravehicular Mobility Unit (EMU): Human Performance Issues During EVA," Master of Science Thesis, Massachusetts Institute of Technology, Cambridge, MA, 1997.

32. Sanders, M. S. and McCormick, E. J., Human Factors in Engineering and Design, 7th ed. McGraw-Hill, New York, 1993.

33. Schmidt, P. An Investigation of Space Suit Mobility With Applications to EVA Operations. Ph.D. Dissertation, Massachusetts Institute of Technology, September, 2001.

34. Schmidt, P., Newman, D., Hodgson, E., "Modeling Space Suit Mobility: Applications to Design and Operations", International Conference on Environmental Systems, Orlando, FL, July, 2001.

35. Tao, G and Kokotovic, P,. Adaptive Control of Systems with Actuator and Sensor Nonlinearities. Wiley, New York, 1996.

36. Wang, X. and Verriest, J. P., "A Geometric Algorithm to Predict the Arm Reach Posture for Computer-aided Ergonomic Evaluation," The Journal of Visualization and Computer Animation, Vol. 9, 1998, pp. 33-47.

37. Webb G.V., Kurdila A.J. and Lagoudas D.C., "Adaptive Hysteresis Model for Model Reference Control with Actuator Hysteresis," Journal of Guidance, Control, and Dynamics, Vol. 23, No. 3 p.459, 2000.